Adiabatic theory of strong-field ionization of molecules including nuclear motion

Jens Svensmark,[1] Oleg I. Tolstikhin,[2] and Toru Morishita[1]
[1]*Institute for Advanced Science, The University of Electro-Communications, 1-5-1 Chofu-ga-oka, Chofu-shi, Tokyo 182-8585, Japan*
[2]*Moscow Institute of Physics and Technology, Dolgoprudny 141700, Russia*

(Received 23 February 2020; accepted 9 April 2020; published 12 May 2020)

The adiabatic theory of strong-field ionization of molecules with internuclear motion included into consideration is developed. Two adiabatic regimes in terms of the electronic, nuclear, and laser field timescales are considered. In the first regime, field is the slowest; that is, its timescale is much larger than the electronic and nuclear timescales. The corresponding theory generalizes the adiabatic theory of strong-field ionization of atoms and molecules with frozen nuclei [Phys. Rev. A **86**, 043417 (2012)] by treating the internuclear motion on equal footing with the electronic motion. In the second regime, the active electron is the fastest; that is, its timescale is much smaller than that of the nuclei and laser field. The corresponding theory naturally involves the Born-Oppenheimer approximation. The two versions of the adiabatic theory are validated by comparing their predictions with accurate numerical results obtained by solving the time-dependent Schrödinger equation (TDSE) for a model diatomic molecule with one electronic and one internuclear degree of freedom. The adiabatic results are shown to converge to the TDSE results uniformly with respect to the laser field amplitude both in tunneling and over-the-barrier ionization regimes. Two applications of the theory to the analysis of strong-field effects associated with the internuclear motion are discussed.

DOI: 10.1103/PhysRevA.101.053422

I. INTRODUCTION

Nuclear motion in molecules interacting with intense laser pulses affects electronic dynamics, which is reflected in strong-field ionization observables—photoelectron momentum distributions (PEMDs) and high-order harmonic generation (HHG) spectra—and can be used for ultrafast imaging of molecular structure. Furthermore, resolving the observables with respect to the final state of the molecular ion or its dissociated fragments may provide access to more detailed information on the correlated electron-nuclear dynamics. Thus, the inclusion of the nuclear motion into consideration suggests a natural direction for expanding the research area in strong-field physics [1].

The numerical solution of the time-dependent Schrödinger equation (TDSE) has proven to be a powerful tool for studying highly nonperturbative strong-field processes. In the early theoretical papers where the internuclear motion was treated on an equal footing with the electronic motion [2–7], the TDSE was solved for different reduced dimensionality models describing the ionization and dissociation of H_2^+ in a strong laser field. In Refs. [2,3,5,6], the initial condition for the TDSE was specified in the Born-Oppenheimer approximation (BOA), while in Refs. [4,7] an exact three-body initial state was used. These studies focused primarily on the analysis of the nuclear wave-packet dynamics visualizing the dissociation process. In addition, in Ref. [5] populations of the different bound electronic and vibrational states of H_2^+ were calculated by projecting the time-dependent wave function onto the corresponding states in the BOA, and in Ref. [6] separate electronic and nuclear kinetic energy spectra were evaluated by Fourier transforming the wave function at the end of the pulse in the corresponding coordinate. The early studies were followed by numerous applications of the TDSE supplemented with other theoretical techniques to the prediction and analysis of various strong-field effects associated with the internuclear motion. This includes discussions of the Coulomb explosion imaging [8], carrier-envelope-phase-induced asymmetry in the dissociation products [9,10], isotope effect in HHG spectra [11], dynamic interference in the Coulomb explosion [12], vibrational excitation [13], field-driven electronic dynamics during dissociation [14], the joint energy spectrum of the electronic and nuclear fragments [15] and its dependence on the laser intensity [16], the appearance of even-order harmonics in HHG radiation from homonuclear diatomic molecules [17], the effect of exceptional points of molecules in an electric field on the dissociation dynamics [18], post-laser-pulse oscillations induced by excitation above the dissociation threshold [19], etc. The effects discussed in Refs. [9,10], [11], [12], and [15,16] were also investigated experimentally in Refs. [20], [21], [22], and [23–25], respectively. Note that in most of the TDSE studies to date observables are calculated by projecting onto final molecular states in the BOA. This approximation greatly facilitates calculations, especially for the dissociative ionization process involving double continua [15], since constructing exact molecular scattering states is a nontrivial problem in itself, but also introduces an uncontrollable error. In this respect, calculations including internuclear motion have not yet advanced to the stage of TDSE calculations for one-electron atoms [26–30] and molecules with frozen nuclei [31,32] and two-electron atoms [33,34] in which exact scattering states are used to extract observables.

Tunneling ionization deserves special mention as the first step for all strong-field phenomena. In the adiabatic regime, tunneling proceeds as if the ionizing field were static and equal to the instantaneous laser field; this enables one to

treat this step within a time-independent framework separately from the rest of the process. Studies of the effect of the internuclear motion on tunneling ionization of molecules were initiated in Ref. [35], where the relative populations of the vibrational states of H_2^+ resulting from tunneling ionization of H_2 were measured experimentally and calculated theoretically. Later, the isotope effect on the total ionization rate of molecules was predicted theoretically [36] and confirmed experimentally [37]. The analysis in Refs. [35,36] was based on the BOA. The applicability of this approximation in the theory of tunneling ionization was revisited in Ref. [38]. It was shown that the BOA breaks down at sufficiently weak fields, while the weak-field asymptotic theory (WFAT) [39], on the contrary, works well in this case. The complementarity of the WFAT and BOA in the theory of tunneling ionization of molecules was analyzed and illustrated by calculations in Refs. [40–43].

Typical lasers used in strong-field experiments operate in the near-infrared range at frequencies $\omega \sim 0.057$ a.u. (wavelengths ~800 nm). The corresponding laser period $2\pi/\omega \sim 110$ a.u. by far exceeds the characteristic time $2\pi/I_p \sim 12.6$ a.u. of the electronic motion in atoms, where $I_p \sim 0.5$ a.u. is the ionization potential. In Ref. [44], the adiabatic theory of strong-field ionization based on the asymptotic expansion in a small parameter given by the ratio of electronic and field timescales was developed. The power of this theory was demonstrated by predicting a shift of the maximum of PEMDs generated by circularly polarized pulses [30], which has been observed experimentally [45], unraveling target structure information from the strong-field photoelectron holography pattern [46], developing a theory of rescattering [32,47] which has been confirmed by experiments with atoms [48] and molecules [49,50], and suggesting a method for molecular orbital imaging [51]. Recent developments in generating intense few-cycle pulses are heading toward the midinfrared [52] and even the terahertz [53] range. Solving the TDSE for such pulses becomes prohibitively difficult, even for atomic targets. Meanwhile, the adiabatic theory can be implemented with the same ease and its predictions become more accurate as the laser wavelength grows.

The goal of this paper is to generalize the adiabatic theory [44] by including the internuclear motion into consideration. In general, the adiabatic approximation relies on the presence of different timescales in the system. The theory developed in Ref. [44] relies on the small ratio of electronic and laser field timescales, which enables one to treat strong-field ionization of atoms and molecules with frozen nuclei. In molecules with moving nuclei, additional timescales characterizing the nuclear motion appear. In this paper, we include only the internuclear motion, as was also done in all the TDSE calculations mentioned above, leaving rotations to future studies. Thus, we deal with a system having three timescales. The structure of the theory depends on the relation between these timescales. We develop two versions of the theory applicable in regimes which seem to be most relevant for applications in strong-field physics. We also validate the theories and illustrate their quantitative performance by comparing their predictions with the results of TDSE calculations for a model diatomic molecule with one electronic and one internuclear degree of freedom treated previously within a time-independent framework [38,40–42].

The paper is organized as follows. In Sec. II, we describe the model and define observables in terms of the solution to the TDSE. We use exact three-body states for both the initial condition for the TDSE and observables, which is a strong point of the present TDSE calculations. In Sec. III, the TDSE is reformulated in an integral form more convenient for deriving the adiabatic asymptotics of the wave function. In Sec. IV, a flux formula for the ionization amplitude is obtained, which is more convenient for deriving the adiabatic asymptotics of the ionization observables. The two versions of the adiabatic theory mentioned above are developed in Sec. V. In Sec. VI, they are validated by comparison with the TDSE calculations. In Sec. VII, two applications illustrating the usefulness of the adiabatic theory are discussed. Section VIII concludes the paper. The numerical techniques used in the calculations are described in the Appendix.

II. BASIC EQUATIONS

A. Model

Following Refs. [38,40–42], we consider a model one-dimensional (1D) molecule consisting of two identical nuclei with masses $m_1 = m_2 = M$ and charges $q_1 = q_2 = 1/2$ and one active electron with mass $m_3 = 1$ and charge $q_3 = -1$ (atomic units are used throughout the paper). The molecule is treated in its center-of-mass frame, so the nuclear x_1 and x_2 and electronic x_3 coordinates satisfy $M(x_1 + x_2) + x_3 = 0$. Its Hamiltonian is given by

$$H_0 = -\frac{1}{2\mu}\frac{\partial^2}{\partial R^2} - \frac{1}{2m}\frac{\partial^2}{\partial x^2} + U_{\rm ion}(R) + V(x;R), \qquad (1)$$

where $R = x_2 - x_1$ and $x = x_3 - (x_1 + x_2)/2 = x_3/m$ are Jacobi coordinates and $\mu = M/2$ and $m = 2M/(2M+1)$ are the corresponding reduced masses. The potential $U_{\rm ion}(R)$ models the internuclear interaction in the molecular ion. We assume that the nuclei cannot pass through each other, so the system is considered in the region $R \geqslant 0$ with zero boundary condition at $R = 0$. In addition, in this paper we assume that the molecular ion has a purely discrete spectrum of eigenstates defined by

$$\left[-\frac{1}{2\mu}\frac{d^2}{dR^2} + U_{\rm ion}(R) - \varepsilon_v\right]\chi_v(R) = 0, \qquad (2a)$$

$$\chi_v(0) = \chi_v(R \to \infty) = 0, \qquad (2b)$$

where $v = 0, 1, \ldots$ is the vibrational quantum number, and we impose zero boundary condition also at $R \to \infty$. This means that the molecule cannot dissociate. Our previous studies [38,40] showed that even without dissociation the system described by Eq. (1) provides an instructive model for investigating effects of internuclear motion on the dynamics of ionization in an external electric field. The dissociation channel can be included into the present theory later, as was done in the stationary case in Refs. [41,42]. The potential $V(x;R)$ describes the interaction of the active electron with the molecular ion. It is considered as a function of the Jacobi coordinate x which parametrically depends on the internuclear distance R. In the present homonuclear case, this potential

is symmetric, $V(x;R) = V(-x;R)$. We assume that it has a finite range or vanishes sufficiently rapidly as $|x|$ grows at a given R, which is required for the applicability of the approach developed in Ref. [44]. In the illustrative calculations reported below, the functions $U_{\rm ion}(R)$ and $V(x;R)$ are chosen to model the Born-Oppenheimer (BO) potentials of $H_2{}^+$ and H_2; their explicit forms are given in Sec. VI A.

To define observables, we need to introduce a complete set of eigenstates of H_0. All molecular wave functions considered below satisfy zero boundary conditions at $R = 0$ and $R \to \infty$, so we indicate explicitly only the asymptotic boundary conditions at $|x| \to \infty$. The bound states are defined by

$$(H_0 - E_n)\Phi_n(x,R) = 0, \tag{3a}$$

$$\Phi_n(x,R)|_{|x|\to\infty} = 0, \tag{3b}$$

where $n = 0, 1, \ldots$ enumerates the states in increasing order of their energy E_n. The eigenfunctions $\Phi_n(x,R)$ are assumed to be real. These states lie below the boundary of the electronic continuum ε_0. The *in* (+) and *out* (−) scattering states having an incident wave with momentum k in the entrance vibrational channel v satisfy

$$[H_0 - E_v(k)]\Phi_v^{(\pm)}(x,R;k) = 0, \tag{4}$$

where

$$E_v(k) = \frac{k^2}{2m} + \varepsilon_v. \tag{5}$$

We consider these states in the whole range of the incident momentum, $-\infty < k < \infty$, with positive and negative k corresponding to electrons impinging on the molecular ion from the negative and positive ends of the x axis, respectively. The boundary conditions for the *in* states are specified by

$$\Phi_v^{(+)}(x,R;k>0) = \begin{cases} \sum_{v'} \sqrt{\frac{k}{k_{v'}}} e^{ik_{v'}x} \chi_{v'}(R) S^+_{v'v}(k), & x \to +\infty, \\ e^{ikx}\chi_v(R) - \sum_{v'} \sqrt{\frac{k}{k_{v'}}} e^{-ik_{v'}x} \chi_{v'}(R) S^-_{v'v}(k), & x \to -\infty, \end{cases} \tag{6a}$$

and

$$\Phi_v^{(+)}(x,R;k<0) = \begin{cases} e^{ikx}\chi_v(R) - \sum_{v'} \sqrt{\frac{|k|}{k_{v'}}} e^{ik_{v'}x} \chi_{v'}(R) S^+_{v'v}(k), & x \to +\infty, \\ \sum_{v'} \sqrt{\frac{|k|}{k_{v'}}} e^{-ik_{v'}x} \chi_{v'}(R) S^-_{v'v}(k), & x \to -\infty, \end{cases} \tag{6b}$$

where $k_{v'} = \sqrt{k^2 + 2m(\varepsilon_v - \varepsilon_{v'})} \geqslant 0$, $S^{\pm}_{v'v}(k)$ is the scattering matrix, its superscript indicates the direction of propagation of the outgoing wave in the exit channel v', and the summations run over all open exit channels with $\varepsilon_{v'} < E_v(k)$. In the present homonuclear case, the scattering matrix satisfies $S^-_{v'v}(-k) = S^+_{v'v}(k)$. The *out* states are given in terms of the corresponding *in* states by [54]

$$\Phi_v^{(-)}(x,R;k) = [\Phi_v^{(+)}(x,R;-k)]^*. \tag{7}$$

Note that k is the momentum conjugate to the Jacobi coordinate x. For a given k, the momentum of the electron conjugate to its coordinate $x_3 = mx$ is $k_3 = k/m$. It is convenient to consider the scattering states and the PEMDs defined below as functions of the Jacobi momentum k instead of the electronic momentum k_3. In the BO limit $M \to \infty$ we have $m \to 1$, so the two momenta coincide. We construct molecular eigenstates by solving Eqs. (3) and (4) numerically without any approximations using a procedure described in the Appendix.

B. Time-dependent Schrödinger equation and observables

The molecule interacts with an external time-dependent electric field $F(t)$ representing a laser pulse. Its dipole moment in the center-of-mass frame is $(x_1 + x_2)/2 - x_3 = -x$. Thus, the TDSE describing the system in the dipole approximation and length gauge reads

$$i\frac{\partial}{\partial t}\Psi(x,R,t) = [H_0 + F(t)x]\Psi(x,R,t). \tag{8}$$

Note that the nuclei do not interact with the field in the homonuclear case. The field satisfies $F(t \to \pm\infty) = 0$, and hence the initial condition for Eq. (8) and observables can be expressed in terms of the eigenstates of H_0. We assume that the molecule is initially in the ground state, so the initial condition is

$$\Psi(x,R,t \to -\infty) = \Phi_0(x,R)e^{-iE_0 t}. \tag{9}$$

Observables can be extracted from the solution to Eqs. (8) and (9) at $t \to \infty$, after the pulse is over. The probability for the molecule to remain in a bound state is given by

$$P_n = \left| \int_0^\infty dR \int_{-\infty}^\infty dx\, \Phi_n(x,R)\Psi(x,R,t) \right|^2_{t\to\infty}. \tag{10}$$

All the other observables can be expressed in terms of the ionization amplitude

$$I_v(k) = e^{iE_v(k)t} \int_0^\infty dR \int_{-\infty}^\infty dx\, \Phi_v^{(-)*}(x,R;k)\Psi(x,R,t) \Big|_{t\to\infty}. \tag{11}$$

The partial PEMD describing the process in which an electron is released with momentum k/m while the molecular ion is left in a vibrational state v is given by

$$P_v(k) = |I_v(k)|^2. \tag{12}$$

This is the most detailed characteristic of ionization. Using it, we can define appropriate integral characteristics. The probability of ionization into a given vibrational

channel is

$$P_v^{\rm ion} = \int_{-\infty}^{\infty} P_v(k)\,\frac{dk}{2\pi}. \tag{13}$$

The total PEMD describing the release of an electron with momentum k/m, irrespective of the final state of the molecular ion, is

$$P(k) = \sum_v P_v(k). \tag{14}$$

Finally, the total ionization probability can be calculated using either of

$$P_{\rm ion} = \sum_v P_v^{\rm ion} = \int_{-\infty}^{\infty} P(k)\,\frac{dk}{2\pi}. \tag{15}$$

The unitarity of the evolution described by Eq. (8) ensures that

$$\sum_n P_n + P_{\rm ion} = 1. \tag{16}$$

We solve Eqs. (8) and (9) and calculate the observables numerically without any approximations, as described in the Appendix. This provides exact (within the numerical accuracy) results used for validating the adiabatic theory.

III. INTEGRAL FORM OF THE TIME-DEPENDENT SCHRÖDINGER EQUATION

For developing the theory, it is convenient to rewrite the TDSE (8) in an integral form [44]. Let us introduce a retarded Green's function defined by

$$\left[i\frac{\partial}{\partial t} + \frac{1}{2\mu}\frac{\partial^2}{\partial R^2} + \frac{1}{2m}\frac{\partial^2}{\partial x^2} - U_{\rm ion}(R) - F(t)x\right] \times G(x,R,t;x',R',t') = \delta(t-t')\delta(x-x')\delta(R-R'), \tag{17a}$$

$$G(x,R,t;x',R',t')|_{t<t'} = 0. \tag{17b}$$

Here, we have retained the internuclear and electron-field interactions, which allow separation of the variables x and R, but omitted the potential $V(x;R)$, which couples the electronic and nuclear degrees of freedom. The solution to Eq. (17) can be expressed as a product of retarded Green's functions for the electronic and nuclear subsystems,

$$G(x,R,t;x',R',t') = iG_x(x,t;x',t')G_R(R,R',t-t'). \tag{18}$$

The electronic Green's function satisfies

$$\left[i\frac{\partial}{\partial t} + \frac{1}{2m}\frac{\partial^2}{\partial x^2} - F(t)x\right]G_x(x,t;x',t') = \delta(t-t')\delta(x-x') \tag{19}$$

and is given by [55]

$$G_x(x,t;x',t') = e^{-3i\pi/4}\theta(t-t')\sqrt{\frac{m}{2\pi(t-t')}}\,e^{i\mathcal{S}(x,t;x',t')}, \tag{20}$$

where $\mathcal{S}(x,t;x',t')$ is the classical action accumulated along a trajectory connecting the space-time points (x',t') and (x,t). Let us introduce a reference trajectory with the velocity $v(t)$ and coordinate $x(t)$ defined by

$$m\dot v(t) = -F(t), \quad \dot x(t) = v(t), \tag{21a}$$

$$v(t\to-\infty) = x(t\to-\infty) = 0. \tag{21b}$$

In terms of this trajectory, the action in Eq. (20) is given by [44,56]

$$\frac{1}{m}\mathcal{S}(x,t;x',t') = v(t)x - v(t')x' + \frac{[x(t)-x(t')-(x-x')]^2}{2(t-t')} - \frac{1}{2}\int_{t'}^{t} v^2(t'')dt''. \tag{22}$$

Alternatively, the function (20) can be expanded in Volkov states,

$$G_x(x,t;x',t') = -i\theta(t-t')\int_{-\infty}^{\infty} e^{i\mathcal{S}(x,t;k)-i\mathcal{S}(x',t';k)}\,\frac{dk}{2\pi}. \tag{23}$$

Here $\mathcal{S}(x,t;k)$ is the classical action for a trajectory passing through the point (x,t) and having the asymptotic momentum k [44],

$$\mathcal{S}(x,t;k) = mu_i(t,k)x - \mathcal{S}(t;k), \tag{24a}$$

$$\mathcal{S}(t;k) = \frac{k^2t}{2m} - \frac{m}{2}\int_t^{\infty}\left[u_i^2(t',k) - (k/m)^2\right]dt', \tag{24b}$$

where $u_i(t,k)$ is the initial velocity of the trajectory at time t,

$$u_i(t,k) = k/m - v_\infty + v(t), \tag{25}$$

and $v_\infty = v(t\to\infty)$. We mention that to extend the present theory to potentials $V(x;R)$ with a Coulomb tail, the approach developed in Ref. [57] may prove useful. The nuclear Green's function satisfies

$$\left[i\frac{\partial}{\partial t} + \frac{1}{2\mu}\frac{\partial^2}{\partial R^2} - U_{\rm ion}(R)\right]G_R(R,R',t) = \delta(t)\delta(R-R'). \tag{26}$$

It can be expanded in terms of the solutions to Eq. (2),

$$G_R(R,R',t) = -i\theta(t)\sum_v e^{-i\varepsilon_v t}\chi_v(R)\chi_v(R'). \tag{27}$$

Having thus constructed the solution to Eq. (17), we can rewrite Eq. (8) as

$$\Psi(x,R,t) = \int_{-\infty}^{t}dt'\int_0^{\infty}dR'\int_{-\infty}^{\infty}dx'\,G(x,R,t;x',R',t') \times V(x';R')\Psi(x',R',t'). \tag{28}$$

This is the integral form of Eq. (8) we need. The absence of an inhomogeneous term in this equation is a consequence of the initial condition (9).

IV. ALTERNATIVE EXPRESSIONS FOR THE IONIZATION AMPLITUDE

In the following analysis, we focus on ionization processes described by the ionization amplitude (11). This amplitude can be expressed in different forms [44]. We can rewrite

Eq. (11) as

$$I_v(k) = e^{iE_v(k)t}\int_0^\infty dR\int_{-\infty}^\infty dx\, e^{-ikx}\chi_v(R) \times (1-\hat{P}_b)\Psi(x,R,t)\Big|_{t\to\infty}, \tag{29}$$

where $\hat{P}_b$ is the projector onto the subspace of bound states of the unperturbed molecule. If we insert Eq. (28) with the electronic Green's function given by Eq. (23) into the first term on the right-hand side of Eq. (29), this term takes the form

$$-i\int_{-\infty}^t dt'\int_0^\infty dR\int_{-\infty}^\infty dx\, e^{i\varepsilon_v t' - i\mathcal{S}(x,t';k)}\chi_v(R) \times V(x;R)\Psi(x,R,t')\Big|_{t\to\infty}. \tag{30}$$

The part of $\Psi(x,R,t)$ belonging to the continuous spectrum of H_0 represents electrons liberated from the molecule. Such electrons fly away from the parent molecular ion after the laser pulse is over, so

$$V(x;R)(1-\hat{P}_b)\Psi(x,R,t)\big|_{t\to\infty} = 0. \tag{31}$$

Using this, the second term in Eq. (29) can be rewritten as

$$-i\int_t^\infty dt'\int_0^\infty dR\int_{-\infty}^\infty dx\, e^{i\varepsilon_v t' - i\mathcal{S}(x,t';k)}\chi_v(R) \times V(x;R)\Psi(x,R,t')\Big|_{t\to\infty}. \tag{32}$$

Combining Eqs. (30) and (32) gives

$$I_v(k) = -i\int_{-\infty}^\infty dt\int_0^\infty dR\int_{-\infty}^\infty dx\, e^{i\varepsilon_v t - i\mathcal{S}(x,t;k)}\chi_v(R) \times V(x;R)\Psi(x,R,t). \tag{33}$$

Inserting here Eq. (8) and integrating by parts, we obtain yet another expression,

$$I_v(k) = \int_{-\infty}^\infty dt\int_0^\infty dR\, e^{i\varepsilon_v t}\chi_v(R)[j(x\to\infty,R,t) - j(x\to-\infty,R,t)], \tag{34}$$

where

$$j(x,R,t) = -\frac{i}{2m}\left[e^{-i\mathcal{S}(x,t;k)}\frac{\partial}{\partial x}\Psi(x,R,t) - \Psi(x,R,t)\frac{\partial}{\partial x}e^{-i\mathcal{S}(x,t;k)}\right] \tag{35}$$

is the ionization flux. Equations (11), (29), (33), and (34) give different exact representations for the ionization amplitude. While Eq. (11) is more suitable for numerical calculations, for deriving adiabatic asymptotics of $I_v(k)$ it is more convenient to use Eq. (34); see Ref. [44].

V. ADIABATIC APPROXIMATIONS

The system under consideration has three different timescales. The first timescale T_e characterizes the electronic motion. We assume that $T_e \sim 1$ (in atomic units), which is the case for molecules in the ground electronic state. The second timescale T_n characterizes the internuclear vibrational motion. It depends on the nuclear mass M and for large M grows as $T_n \sim M^{1/2}$. In this paper, we consider nuclear masses in a wide range from $M \sim 1$ to $M \gg 1$, so T_n varies from $T_n \sim 1$ to $T_n \gg 1$. Finally, the third timescale T_f characterizes the laser field. It is externally controllable and can be varied by varying the laser wavelength. We assume that $T_f \gg 1$, which is of main interest for applications in strong-field physics. In summary, we consider the situation in which $T_e \ll T_f$ and the relation between T_e and T_n varies from $T_e \sim T_n$ to $T_e \ll T_n$. Note that this does not fix the relation between T_n and T_f. The relation between all three timescales is determined by any two of their ratios, e.g., T_f/T_e and T_n/T_e. In this section, we develop two adiabatic approximations (AA) which apply in the different regions of the plane of these ratios (see Fig. 1) and then discuss their compatibility.

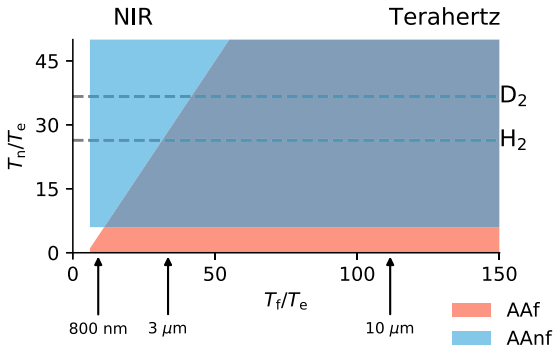

FIG. 1. Illustration of the regions of applicability of AAf [Eq. (36), the wedge-shaped (red) shaded region] and AAnf [Eq. (58), the rectangular (blue) shaded region] in the plane of timescale ratios T_f/T_e and T_n/T_e. In this figure, the electronic timescale is chosen as $T_e = 2\pi/I_p = 12.6$, where $I_p = 0.5$. The nuclear timescale is defined by $T_n = 2\pi/\Delta E_n$, where ΔE_n is the energy difference between the ground and first exited vibrational states of the molecule. We have $T_n = 331$ and 461 for H_2 and D_2, respectively [58]; the corresponding ratios T_n/T_e are shown by dashed lines. The field timescale is $T_f = 2\pi/\omega$, where ω is the laser frequency; the ratios T_f/T_e for several characteristic wavelengths from near-infrared (NIR) to terahertz range are indicated.

A. Field is the slowest

We first consider the limit in which the field varies slowly on timescales of electronic and nuclear motions, that is,

$$\max(T_e, T_n) \ll T_f. \tag{36}$$

This condition holds in the wedge-shaped (red) shaded region in Fig. 1. Let us introduce the corresponding adiabatic parameter

$$\epsilon_f = \max\left(\frac{T_e}{T_f}, \frac{T_n}{T_f}\right). \tag{37}$$

The adiabatic approximation in the region (36) amounts to the asymptotics for $\epsilon_f \to 0$. This version of the adiabatic theory for the present three-timescale molecular system will be referred to as AAf. It generalizes the adiabatic theory for two-timescale atomic systems developed in Ref. [44] by

including the internuclear motion on an equal footing with the electronic motion. In the derivation below, we follow Ref. [44].

1. Molecular Siegert states

In the limit $\epsilon_f \to 0$, the solution to the TDSE (8) and the observables can be expressed in terms of a Siegert state (SS) of the molecule in a static electric field [44]. The SS is the solution to

$$[H_0 + Fx - E_0(F)]\Phi_0(x, R; F) = 0, \tag{38}$$

satisfying the outgoing-wave boundary conditions

$$\Phi_0(x, R; F) = \begin{cases} \sum_v f_v(F) e(x, E(F) - \varepsilon_v)\chi_v(R), & x \to -s\infty, \\ 0, & x \to +s\infty, \end{cases} \tag{39}$$

where $s = \mathrm{sgn}(F)$ and

$$e(x, E) = \frac{m^{1/4}}{(2|Fx|)^{1/4}} \times \exp\left[i\frac{(2m)^{1/2}}{|F|}\left(\frac{2}{3}|Fx|^{3/2} + E|Fx|^{1/2}\right)\right]. \tag{40}$$

Equations (38) and (39) constitute an eigenvalue problem. The subscript 0 indicates the solution which originates from the initial ground state of the molecule as the electric field F is turned on, that is, the one satisfying

$$E_0(F)|_{F\to 0} = E_0, \quad \Phi_0(x, R; F)|_{F\to 0} = \Phi_0(x, R). \tag{41}$$

For $F \neq 0$, the SS eigenvalue is complex,

$$E_0(F) = \mathcal{E}_0(F) - \tfrac{i}{2}\Gamma_0(F), \tag{42}$$

and defines the Stark-shifted energy $\mathcal{E}_0(F)$ and the rate of tunneling or over-the-barrier static-field ionization $\Gamma_0(F)$ of the state. The SS eigenfunction is also complex and normalized by

$$\int_0^\infty dR \int_{-\infty}^\infty dx\, \Phi_0^2(x, R; F) = 1. \tag{43}$$

Note that there is no complex conjugation in this equation, which is a general property of the theory of SSs [59–61]. The coefficients $f_v(F)$ in Eq. (39) are the channel ionization amplitudes. The normalization coefficient in Eq. (40) is chosen such that in the weak-field limit the ionization rate is given by

$$\Gamma_0(F)|_{|F|\to 0} = \sum_v |f_v(F)|^2. \tag{44}$$

Let a denote the range of the potential $V(x; R)$ in x for the interval of R where the eigenfunction $\Phi_0(x, R; F)$ is localized. Then we can specify the boundary condition (39) as

$$\Phi_0(x, R; F)|_{x\ll -a} = e^{-i\pi/12} 2\pi^{1/2} m^{1/3} (2F)^{-1/6} \times \sum_v f_v(F)\,\mathrm{Ai}(\zeta)\chi_v(R), \tag{45a}$$

$$\zeta = e^{-i\pi/3}(2m)^{1/3}F^{-2/3}[E_0(F) - \varepsilon_v - Fx], \tag{45b}$$

where $\mathrm{Ai}(z)$ is the Airy function and, for definiteness, we have assumed that $F > 0$. In the region $x \ll \min(-a, x_v)$, where $x_v = -|E_0(F) - \varepsilon_v|/F$ is the turning point for the motion in x in channel v, Eq. (45a) reduces to Eq. (39).

Molecular SSs in the present model were studied in Refs. [38,40–42]. Here we solve Eqs. (38) and (39) using numerical techniques developed therein. This yields functions $E_0(F)$ and $f_v(F)$ needed to implement AAf.

2. Wave function

The asymptotics of the solution to Eq. (8) for $\epsilon_f \to 0$ is given by a sum of adiabatic and rescattering parts [44],

$$\Psi(x, R, t) = \Psi_a(x, R, t) + \Psi_r(x, R, t). \tag{46}$$

The adiabatic part $\Psi_a(x, R, t)$ describes a state in which the electron remains quasibound. This state adjusts itself to the instantaneous value of the laser field $F(t)$ and adiabatically follows its variation in time. The leakage of electrons in this state is the source of electrons liberated from the molecule. The rescattering part $\Psi_r(x, R, t)$ describes recollision of such electrons with the molecular ion as they return to it being driven by the field. Equation (46) holds inside a quasistationary zone $|x| \ll X(t)$, where $X(t) = |F(t)|T_f^2 = O(\epsilon_f^{-2})$ [44]. In this zone, $\Psi_a = O(\epsilon_f^0)$ and for the present 1D case $\Psi_r = O(\epsilon_f^{1/2})$, which enables one to distinguish the two terms in Eq (46). We mention that in the 3D case $\Psi_r = O(\epsilon_f^{3/2})$ [44], which means that the 1D model exaggerates the relative role of rescattering. Thus, in the limit $\epsilon_f \to 0$, the adiabatic part is the leading-order term in Eq. (46). In this paper, we restrict our treatment to the leading-order approximation within AAf described by the adiabatic part of the wave function. Effects of rescattering can be included following [44]; we leave this to future studies.

The function $\Psi_a(x, R, t)$ is sought in the form [44]

$$\Psi_a(x, R, t) = \Phi_0(x, R; t)e^{-is_0(t)}, \tag{47}$$

where

$$s_0(t) = E_0 t + \int_{-\infty}^t [E_0(t') - E_0]\,dt'. \tag{48}$$

The functions $E_0(t)$ and $\Phi_0(x, R; t)$ introduced here are assumed to be slow functions of time in the sense that their derivatives in t are $O(\epsilon_f^1)$. To find them, we substitute Eq. (47) for the wave function in Eq. (28). All factors in the integrand as functions of t' are expanded in $\delta = t - t'$ in the region $\delta \ll T_f = O(\epsilon_f^{-1})$ retaining terms of order $O(\epsilon_f^0)$. We have

$$\Phi_0(x', R'; t') = \Phi_0(x', R'; t) + O\left(\epsilon_f^1\right), \tag{49a}$$

$$s_0(t') = s_0(t) - E_0(t)\delta + O\left(\epsilon_f^1\right). \tag{49b}$$

The action (22) is expanded using $d^n F(t)/dt^n = O(\epsilon_f^n)$,

$$\mathcal{S}(x, t; x', t') = \frac{m(x - x')^2}{2\delta} - \frac{1}{2}F(t)(x + x')\delta - \frac{1}{24m}F^2(t)\delta^3 + O\left(\epsilon_f^1\right). \tag{50}$$

Substituting this into Eq. (28), we obtain an integral equation for $\Phi_0(x, R; t)$ as a function of spatial coordinates x and R,

where the kernel is given by an integral over δ. It can be shown that this equation coincides with the integral form of Eq. (38), where F is substituted by $F(t)$ [44]. We thus obtain

$$E_0(t) = E_0(F(t)), \quad \Phi_0(x, R; t) = \Phi_0(x, R; F(t)). \tag{51}$$

Omitting further details, we mention that to derive the second of these equations, including the normalization coefficient defined by Eq. (43), the above expansions should be extended to terms of order $O(\epsilon_f^1)$ [44]. Equations (47), (48), and (51) define the leading-order term in the asymptotics of the solution to Eq. (28) for $\epsilon_f \to 0$. It can be seen from Eqs. (41) that the function (47) satisfies the initial condition (9).

3. Observables

Within AAf, the observables should be calculated using Eq. (47). Substituting this function into Eq. (10), we obtain the survival probability

$$P_0^f = \exp\left[-\int_{-\infty}^{\infty} \Gamma_0(t)\, dt\right], \tag{52}$$

where $\Gamma_0(t) = \Gamma_0(F(t))$. Probabilities of transitions to excited states with $n > 0$ in this approximation are equal to zero. Such transitions are exponentially suppressed in the limit $\epsilon_f \to 0$ and not accounted for by Eq. (47).

We now evaluate the ionization amplitude using Eq. (34). Substituting Eq. (47) into Eq. (35), the integrand in Eq. (34) contains a factor $e^{iS_a(x,t;k)}$ with the adiabatic action

$$S_a(x, t; k) = -\mathcal{S}(x, t; k) + \varepsilon_v t - s_0(t). \tag{53}$$

In the limit $\epsilon_f \to 0$, the first term here defined by the classical action (24) is $O(\epsilon_f^{-3})$, while the other two terms having quantum origin are $O(\epsilon_f^{-1})$. Since $e^{iS_a(x,t;k)}$ oscillates rapidly, and the other factors in the integrand in Eq. (34) are slow functions of t, the integral over t can be evaluated using the steepest descent method. The saddle points are defined by

$$\frac{\partial S_a}{\partial t} = \frac{m}{2} u_i^2(t, k) + F(t)x + \varepsilon_v - E_0(t) = 0. \tag{54}$$

We evaluate the right-hand side of Eq. (34) at $|x| \gg a$, where the potential $V(x; R)$ can be neglected and Eq. (45a) holds. Let us recall that Eq. (47) holds at $|x| \ll X(t)$. Since $a = O(\epsilon_f^0)$ and $X(t) = O(\epsilon_f^{-2})$, in the limit $\epsilon_f \to 0$ there exists a region $a \ll |x| \ll X(t)$ where both conditions are satisfied. We apply Eq. (34) at $x = O(\epsilon_f^0)$ inside this region. Then the first term in Eq. (54) is $O(\epsilon_f^{-2})$, while the other terms are $O(\epsilon_f^0)$. It can be seen that the saddle points appear in pairs located near the corresponding solution to [44]

$$u_i(t, k) = 0 \quad \to \quad t = t_i(k). \tag{55}$$

We use $t_i(k)$ as a reference point and expand the action (54) in $\delta = t - t_i(k)$,

$$S_a(x, t; k) = \mathcal{S}(t_i; k) + \varepsilon_v t_i - s_0(t_i) + [F(t_i)x + \varepsilon_v - E_0(t_i)]\delta + \frac{1}{6m} F^2(t_i)\delta^3 + O\left(\epsilon_f^1\right), \tag{56}$$

where $\mathcal{S}(t; k)$ is defined by Eq. (24b) and we have omitted the argument of $t_i(k)$. The following derivation parallels that in Ref. [44]. When we substitute Eq. (56) into Eq. (34), the integral over t can be calculated analytically and the result is given in terms of an Airy function. On the other hand, the integral $\int_0^\infty \chi_v(R)\Phi_0(x, R; t_i)\, dR$ appearing in Eq. (34) at $|x| \gg a$ can be also expressed in terms of an Airy function using Eq. (45a). The ionization flux (35) reduces to the Wronskian of the two Airy functions; it does not depend on x, which eliminates the dependence on x of the right-hand side of Eq. (34). We thus obtain

$$I_v^f(k) = e^{i\pi/4}(2\pi)^{1/2} \sum_i \frac{f_v(t_i)}{|F(t_i)|^{1/2}} \times \exp[i\mathcal{S}(t_i, k) + i\varepsilon_v t_i - i s_0(t_i)]. \tag{57}$$

Here $f_v(t) = f_v(F(t))$, where $f_v(F)$ is defined by Eq. (39), and the summation runs over the different solutions to Eq. (55). Equation (57) gives the leading-order term in the asymptotics of the ionization amplitude for $\epsilon_f \to 0$. Using Eq. (57), we obtain all the ionization observables defined in Sec. II B within AAf.

B. Electron is the fastest

We now consider the limit in which the electronic motion is faster compared to the nuclear motion and to how the field varies with time, that is

$$T_e \ll \min(T_n, T_f). \tag{58}$$

This condition holds in the rectangular (blue) shaded region in Fig. 1. The corresponding adiabatic parameter is

$$\epsilon_{nf} = \max\left(\frac{T_e}{T_n}, \frac{T_e}{T_f}\right). \tag{59}$$

The adiabatic approximation in the region (58) is the asymptotics for $\epsilon_{nf} \to 0$. Note, importantly, that this asymptotics implies the BO limit $M \to \infty$, which is used below. Being interested only in the leading-order approximation for $\epsilon_{nf} \to 0$, in this subsection we set $m = 1$. We will refer to this version of the adiabatic theory for the present three-timescale system as AAnf.

1. Electronic Siegert states

In the limit $M \to \infty$ the BOA applies. This suggests that in the limit $\epsilon_{nf} \to 0$ the solution to the TDSE (8) and the observables can be expressed in terms of an electronic SS in a static electric field defined by [compare with the molecular SS defined by Eq. (38)]

$$\left[-\frac{1}{2}\frac{d^2}{dx^2} + V(x; R) + Fx - E_e(R, F)\right]\psi_e(x; R, F) = 0, \tag{60}$$

subject to the outgoing-wave boundary conditions

$$\psi_e(x; R, F) = \begin{cases} f(R, F)e_{m=1}(x, E(R, F)), & x \to -s\infty, \\ 0, & x \to +s\infty, \end{cases} \tag{61}$$

where $s = \mathrm{sgn}(F)$ and $e_{m=1}(x, E)$ is given by Eq. (40) with $m = 1$. This is an eigenvalue problem. Its solutions depend on R as a parameter. We need the solution which originates from the ground electronic state as the electric field F is turned on.

For $F \neq 0$, the SS eigenvalue is complex and can be presented in the form

$$E_e(R,F) = \mathcal{E}_e(R,F) - \tfrac{i}{2}\Gamma_e(R,F), \tag{62}$$

which defines the energy $\mathcal{E}_e(R,F)$ and ionization rate $\Gamma_e(R,F)$ of the state at a given R. The SS eigenfunction is also complex and normalized by

$$\int_{-\infty}^{\infty} \psi_e^2(x;R,F)\,dx = 1, \tag{63}$$

again without complex conjugation, as in Eq. (43). The coefficient $f(R,F)$ in Eq. (61) is the ionization amplitude at a given R. Similar to Eq. (44), in the weak-field limit it is related to the ionization rate by

$$\Gamma_e(R,F)_{|F|\to 0} = |f(R,F)|^2. \tag{64}$$

We solve Eqs. (60) and (61) and calculate functions $E_e(R,F)$ and $f(R,F)$ needed to implement AAnf numerically, as described in the Appendix.

2. Wave function

The asymptotics of the solution to Eq. (8) for $\epsilon_{\rm nf} \to 0$ can be sought in the form

$$\Psi(x,R,t) = \Psi(R,t)\psi_e(x;R,F(t)). \tag{65}$$

This should be viewed as an expansion in electronic SSs [18], where only one term is retained. The electronic factor $\psi_e(x;R,F(t))$ is a slow function of both R and t, while the nuclear factor $\Psi(R,t)$ is assumed to incorporate the main dependence of the molecular wave function on these variables. This justifies Eq. (65) in the spirit of the BOA. We substitute this ansatz into Eq. (8) and neglect all terms containing derivatives of $\psi_e(x;R,F(t))$ in R (BOA, $T_e \ll T_n$) and t (AA, $T_e \ll T_f$). Projecting the resulting equation on $\psi_e(x;R,F(t))$, we obtain a TDSE defining the nuclear factor in Eq. (65),

$$i\frac{\partial}{\partial t}\Psi(R,t) = \left[-\frac{1}{2\mu}\frac{\partial^2}{\partial R^2} + U_{\rm mol}(R,F(t))\right]\Psi(R,t), \tag{66}$$

where

$$U_{\rm mol}(R,F) = U_{\rm ion}(R) + E_e(R,F) \tag{67}$$

is the molecular BO potential in a static field F. To specify the initial condition for Eq. (66), we note that in the limit $M \to \infty$ bound states of the unperturbed molecule [see Eq. (3)] are given by the BOA

$$E_n = E_n^{\rm BO}, \quad \Phi_n(x,R) = \Psi_n(R)\psi_e(x;R,0). \tag{68}$$

Here the energy $E_n^{\rm BO}$ of the state and the nuclear wave function $\Psi_n(R)$ are defined by

$$\left[-\frac{1}{2\mu}\frac{d^2}{dR^2} + U_{\rm mol}(R) - E_n^{\rm BO}\right]\Psi_n(R) = 0, \tag{69}$$

where $U_{\rm mol}(R) = U_{\rm mol}(R,0)$ is the field-free molecular BO potential. These equations only describe states in which the electron is in the ground state; other molecular bound states can be obtained similarly using excited-bound-state solutions to Eq. (60) for $F = 0$. Taking into account Eq. (9), the initial condition for Eq. (66) is

$$\Psi(R, t \to -\infty) = \Psi_0(R)e^{-iE_0^{\rm BO}t}. \tag{70}$$

Equation (65), where the nuclear factor is defined by Eqs. (66) and (70), gives the leading-order approximation to the solution to Eq. (8) for $\epsilon_{\rm nf} \to 0$. Note that for $F \neq 0$ the potential (67) is complex, so the norm of $\Psi(R,t)$ is not conserved. We solve the nuclear TDSE (66) numerically, as described in the Appendix. The solution $\Psi(R,t)$ is also needed to implement AAnf.

3. Observables

Within AAnf, the observables should be calculated using Eqs. (65) and (68). Substituting these functions into Eq. (10), we obtain probabilities of transitions to the different bound molecular states in which the electron is in the ground state,

$$P_n^{\rm nf} = \left|\int_0^{\infty} \Psi_n(R)\Psi(R,t)\,dR\right|^2_{t\to\infty}. \tag{71}$$

Probabilities of transitions to electronically excited states in this approximation are equal to zero. Such transitions are caused by non-BO and nonadiabatic couplings not accounted for by Eqs. (65) and (68).

We now evaluate the ionization amplitude, again using Eq. (34). To this end, we need to discuss the dependence of the nuclear wave function $\Psi(R,t)$ on time. This function can be expanded in terms of the solutions to Eq. (69). Because the molecular BO potential in Eq. (66) depends on t, excited states appear in the expansion during the evolution. The number of states which are efficiently populated does not depend on M, because couplings to higher states decay independently of M as the degree of excitation grows. For such states $E_n^{\rm BO} - E_0^{\rm BO} = O(M^{-1/2})$. Furthermore, the coefficients in the expansion depend on time with a timescale T_f. Let us present $\Psi(R,t)$ in the form

$$\Psi(R,t) = \tilde{\Psi}(R,t)e^{-iE_0^{\rm BO}t}. \tag{72}$$

The above argumentation shows that $\tilde{\Psi}(R,t)$ is a slow function of t in the sense that its derivative in t is $O(\epsilon_{\rm nf}^1)$. In other words, the exponential factor in Eq. (72) incorporates the main dependence of $\Psi(R,t)$ on t in the limit $\epsilon_{\rm nf} \to 0$.

The rest of the derivation proceeds similarly to that in Sec. V A 3. We substitute Eqs. (65) and (72) into Eq. (35). The integral over t in Eq. (34) is calculated using the steepest descent method, with $\tilde{\Psi}(R,t)$ and $\psi_e(x;R,F(t))$ treated as slow functions of t. The result is expressed in terms of an Airy function. The electronic SS is represented by another Airy function which solves Eq. (60) at $|x| \gg a$ and whose asymptotics at $x \to -s\infty$ reduces to Eq. (61). The Wronskian of the two Airy functions does not depend on x, provided that $E_0^{\rm BO} - \varepsilon_v = E_e(R,F)$. This equality holds under the sign of the integral in Eq. (34) in the limit $M \to \infty$ [43]. Indeed, the nuclear wave function $\Psi(R,t)$ is localized in the region $R = R_{\rm mol} + O(M^{-1/4})$, where $R_{\rm mol}$ is the equilibrium internuclear distance giving the position of the minimum of the unperturbed molecular potential $U_{\rm mol}(R)$. On the other hand, the integral over R in Eq. (34) is accumulated in an interval of width $O(M^{-1/2})$ near a turning point R_v of $\chi_v(R)$ defined by $U_{\rm ion}(R_v) = \varepsilon_v$; this fact underlies the well-known reflection

approximation used to calculate Franck-Condon factors [64]. Thus, the integral is negligibly small unless $R_v - R_{\rm mol} = O(M^{-1/4})$. In this case, in the region $R = R_v + O(M^{-1/2})$ we have $U_{\rm mol}(R) = U_{\rm mol}(R_{\rm mol}) + O(M^{-1/2})$ and $E_e(R, F) = E_e(R_v, F) + O(M^{-1/2}) = U_{\rm mol}(R_{\rm mol}) - \varepsilon_v + O(M^{-1/2})$. Taking into account that $E_0^{\rm BO} = U_{\rm mol}(R_{\rm mol}) + O(M^{-1/2})$, we obtain $E_0^{\rm BO} - \varepsilon_v - E_e(R, F) = O(M^{-1/2})$, which proves the above statement. Omitting further details, the final result is

$$I_v^{\rm nf}(k) = e^{i\pi/4}(2\pi)^{1/2} \sum_i \frac{g_v(t_i)}{|F(t_i)|^{1/2}} \exp\left[i\mathcal{S}_{m=1}(t_i, k) + i\varepsilon_v t_i\right], \tag{73}$$

where

$$g_v(t) = \int_0^\infty \chi_v(R) f(R, F(t)) \Psi(R, t)\, dR. \tag{74}$$

Here $\mathcal{S}_{m=1}(t, k)$ is given by Eq. (24b) with $m = 1$, t_i is defined by Eq. (55), and the summation runs over the different solutions to this equation, as in Eq. (57). Equation (73) gives the leading-order term in the asymptotics of the ionization amplitude for $\epsilon_{\rm nf} \to 0$. Using it, we obtain all the ionization observables introduced in Sec. II B within AAnf.

C. Compatibility of the two approximations

The two adiabatic approximations considered above apply simultaneously if the timescales satisfy

$$T_e \ll T_n \ll T_f. \tag{75}$$

This condition is fulfilled in the region where the shaded areas in Fig. 1 overlap. Here we show that the AAf and AAnf ionization amplitudes given by Eqs. (57) and (73), respectively, coincide in this region. This is needed to confirm the consistency of the theory.

On the one hand, for $T_e \ll T_n$ (that is, $M \gg 1$), the molecular SS introduced in Sec. V A 1 can be constructed using the BOA. In the limit $M \to \infty$, the solution to Eq. (38) is given by [40–42]

$$E_0(F) = E_0^{\rm BO}(F), \quad \Phi_0(x, R; F) = \Psi_0(R; F)\psi_e(x; R, F), \tag{76}$$

where the SS energy $E_0^{\rm BO}(F)$ and the nuclear wave function $\Psi_0(R; F)$ are defined by the solution to

$$\left[-\frac{1}{2\mu}\frac{d^2}{dR^2} + U_{\rm mol}(R, F) - E_0^{\rm BO}(F)\right]\Psi_0(R; F) = 0, \tag{77}$$

which originates from the ground-state solution to Eq. (69) as the field F is turned on and $\psi_e(x; R, F)$ is the electronic SS defined by Eq. (60). In addition, in this limit the channel ionization amplitudes characterizing the molecular SS are given in terms of the ionization amplitude at a given R characterizing the electronic SS by (see Eq. (40a) in Ref. [42] and Eq. (49) in Ref. [43])

$$f_v(F) = \int_0^\infty \chi_v(R) f(R, F) \Psi_0(R, F)\, dR. \tag{78}$$

On the other hand, for $T_n \ll T_f$, the solution to Eq. (66) can be obtained using the adiabatic approximation in the form

$$\Psi(R, t) = \Psi_0(R, F(t)) e^{-is_0^{\rm BO}(t)}, \tag{79}$$

where

$$s_0^{\rm BO} = E_0^{\rm BO} t + \int_{-\infty}^t \left[E_0^{\rm BO}(F(t')) - E_0^{\rm BO}\right] dt'. \tag{80}$$

Substituting Eq. (79) into Eq. (74) and comparing with Eq. (78), we obtain

$$f_v(t) e^{-is_0(t)} = g_v(t). \tag{81}$$

This proves that Eqs. (57) and (73) coincide in the region (75).

We conclude this theory section by the following remark. Equations (57) and (73) have been obtained as the leading-order terms in the asymptotics for $\epsilon_{\rm f} \to 0$ and $\epsilon_{\rm nf} \to 0$, respectively. It should be noted that the regions of validity of these results depend on the field strength. Let F_0 denote the characteristic amplitude of $F(t)$. Then Eq. (57) holds under the condition $\epsilon_{\rm f} \ll \min(1, \xi^2)$, where $\xi = F_0/\varkappa^3$, $\varkappa = \sqrt{2I_p}$, and I_p is the ionization potential of the molecule [44], and the validity of Eq. (73) requires $F_0 \gg F_{\rm BO}$, where $F_{\rm BO} = \varkappa_e/T_n$ and $\varkappa_e = \sqrt{-2E_e(R_{\rm mol}, 0)}$ [38]. For fixed timescales, these conditions are violated at sufficiently weak fields. While the former condition can be fulfilled by increasing T_f, independently of the value of F_0, the latter condition indicating the breakdown of the BOA in the theory of tunneling ionization [38] cannot be fulfilled by varying only the timescales. In Fig. 1, we assumed that F_0 is sufficiently large, so that both these conditions are satisfied.

VI. ILLUSTRATIVE CALCULATIONS: VALIDATION OF THE THEORY

In this section, we present illustrative numerical results validating the adiabatic approximations developed above and clarifying the regions of their applicability. All the calculations are performed for pulses with the Gaussian envelope,

$$F(t) = F_0 e^{-\tau^2} f(\tau), \quad \tau = 2t/T, \tag{82}$$

where F_0 is the pulse amplitude, T is the pulse duration, and the function $f(\tau)$ describes the internal shape of the pulse. We will consider half-cycle pulses with

$$f(\tau) = 1 \tag{83}$$

and few-cycle pulses with

$$f(\tau) = \cos n_{\rm oc}\pi\tau = \cos \omega t, \tag{84}$$

where $\omega = n_{\rm oc} 2\pi/T$ and $n_{\rm oc}$ is the number of optical cycles in the pulse. The field timescale T_f for these pulses estimated as the duration of a half-cycle is T and $T/2n_{\rm oc}$, respectively. In the calculations, it is varied by varying the pulse duration T while preserving the pulse shape determined by $f(\tau)$. The nuclear timescale T_n is varied by varying the nuclear mass M. We present results in a wide range of the parameters M, T, and F_0. The TDSE results are obtained by solving Eq. (8) and calculating the observables using equations given in Sec. II B. The AAf and AAnf results are obtained as discussed in Secs. V A and V B, respectively. The numerical procedures used in the calculations are described in the Appendix.

A. Model potentials

Here we define the potentials in Eq. (1). The internuclear interaction in the molecular ion is modeled by

$$U_{\rm ion}(R) = \frac{A}{R^2 + D} + B + CR^2, \tag{85}$$

where the term CR^2 prevents the molecule from dissociating. The parameters in Eq. (85) are chosen to reproduce the electronic ground-state BO potential of H_2^+ near its minimum located at $R_{\rm ion} = 2$. The electron-nuclear interaction is modeled by

$$V(x;R) = V(x + R/2) + V(x - R/2), \tag{86}$$

where

$$V(x) = -\frac{a}{\cosh^2(bx)}. \tag{87}$$

This function rapidly decays at large $|x|$, which complies with the assumption that $V(x;R)$ has a finite range in x. The parameters in Eq. (87) are chosen such that the field-free molecular BO potential $U_{\rm mol}(R)$ reproduces the ground-state BO potential of H_2 near its minimum at the equilibrium internuclear distance $R_{\rm mol} = 1.4$.

In this section, we consider two values of the nuclear mass: light nuclei with $M = 3$ and heavy nuclei with $M = 1836$. The model system corresponding to the light nuclei case may seem to be rather artificial. However, it is worthwhile to consider this case for validating AAf; moreover, it may be relevant for expanding strong-field physics to exotic three-body Coulomb systems such as eee^+ and $pp\mu$; see Ref. [13]. In this case, we use the parameters $A = 0.236$, $B = -0.713$, $C = 0.0135$, $D = 0.195$, $a = 0.53622$, and $b = 0.667$. The more realistic heavy nuclei case models the hydrogen molecule H_2. In this case, we use the same parameters as in Ref. [38], namely, $A = 0.26$, $B = -0.732635$, $C = 0.01625$, $D = 0$, $a = 0.62772$, and $b = 0.857$. The difference between the two sets of parameters is caused by a nonzero value of D in the light nuclei case which is introduced to simplify the numerical procedure (see the Appendix).

The BO potentials for $M = 3$ and 1836 in the present model are shown in Figs. 2 and 3, respectively. The top (red) line shows the ionic potential $U_{\rm ion}(R)$. The bottom (black) line shows the molecular potential $U_{\rm mol}(R)$ in the ground electronic state. The intermediate (blue) line shows the molecular potential in the first excited electronic state. In Fig. 3, for comparison, we have additionally plotted the electronic ground-state BO potentials for real H_2^+ and H_2. Several of the lowest ionic energies ε_v defined by Eq. (2) are shown in the ionic potentials. The solutions to Eqs. (3) and (60) with $F = 0$ are either even or odd with respect to the reflection $x \to -x$. Furthermore, in the present model the potential (86) supports only two bound electronic states, one even ground state and one odd excited state. This enables us to unambiguously assign exact three-body bound states defined by Eq. (3) to BO potentials by their symmetry in x. All bound-state energies of the molecule $E_n < \varepsilon_0$ in the ground and first excited electronic states are shown in the corresponding molecular potentials. The horizontal dotted line indicates the boundary of the electronic continuum ε_0.

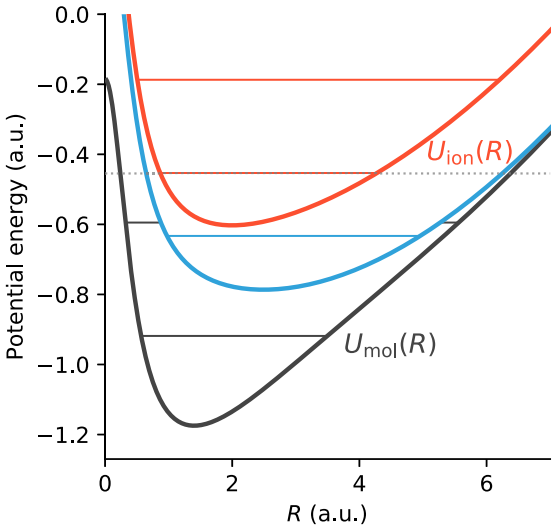

FIG. 2. BO potentials in the present model for light nuclei with $M = 3$. The top (red) line shows the ionic potential $U_{\rm ion}(R)$ with several of the lowest vibrational energies ε_v. The bottom (black) and intermediate (blue) lines show the molecular BO potential $U_{\rm mol}(R)$ for the ground (even in x) and first excited (odd in x) electronic states with all corresponding bound-state molecular energies E_n. The horizontal dotted line indicates the boundary of the electronic continuum ε_0.

SSs are essential building blocks needed to implement the adiabatic approximations. The two-dimensional (2D) molecular SS defined by Eq. (38) provides all the information needed to implement AAf. The energies $\mathcal{E}_0(F)$ and ionization rates $\Gamma_0(F)$ [see Eq. (42)] of this SS in the present model with $M = 3$ and 1836 as functions of field strength

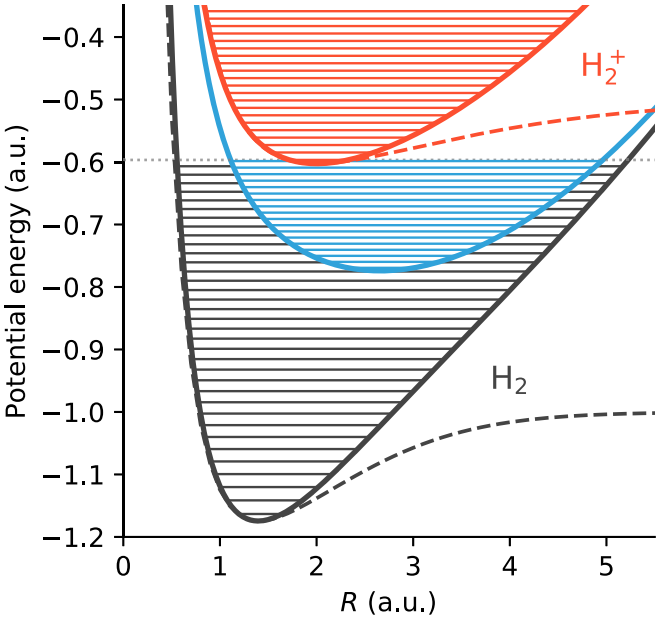

FIG. 3. Similar to Fig. 2, but for heavy nuclei with $M = 1836$. The top (red) and bottom (black) dashed lines show BO potentials for real H_2^+ [62] and H_2 [63].

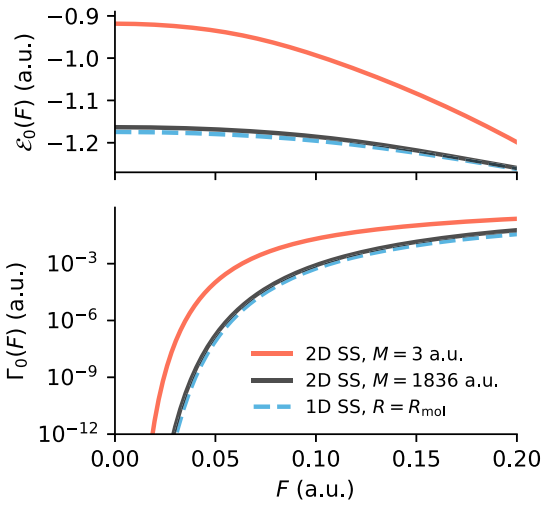

FIG. 4. Solid lines in the top and bottom panels show energies $\mathcal{E}_0(F)$ and ionization rates $\Gamma_0(F)$, respectively, of molecular (2D) SSs in the present model with $M = 3$ (upper red lines) and $M = 1836$ (lower black lines). Dashed (blue) lines in the top and bottom panels show the function $U_{\rm ion}(R_{\rm mol}) + \mathcal{E}_e(R_{\rm mol}, F)$ defined by the energy of the electronic (1D) SS and the corresponding ionization rate $\Gamma_e(R_{\rm mol}, F)$, respectively, calculated in the present model with $M = 1836$ at the equilibrium internuclear distance $R_{\rm mol} = 1.4$.

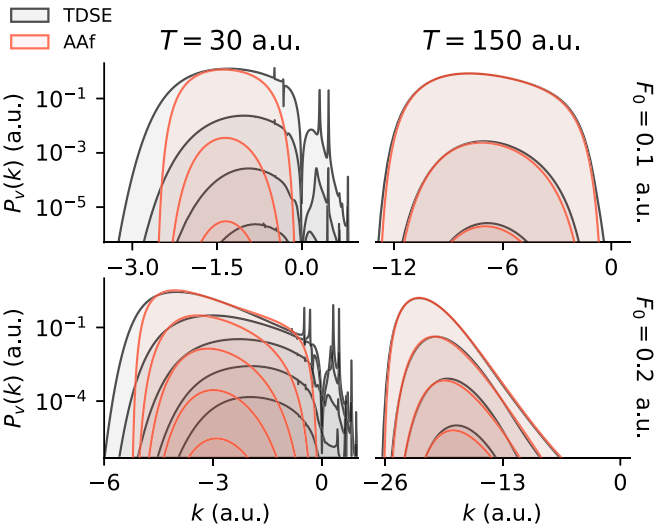

FIG. 5. Partial PEMDs $P_v(k)$ for the light nuclei model ($M = 3$) generated by half-cycle pulses with amplitudes F_0 and durations T indicated in the figure. The TDSE results (darker lines) are obtained from Eq. (12) and the AAf results (lighter lines) are calculated using Eq. (57). The top TDSE and AAf lines in each panel correspond to $v = 0$; the others follow downward in increasing order of v.

are shown by the upper (red) and lower (black) solid lines in Fig. 4, respectively. As M grows, the energy of the SS shifts downward. The ionization potential increases, and the ionization rate therefore decreases, as seen in the figure. The critical field strengths indicating the boundary between tunneling and over-the-barrier ionization regimes estimated from the condition $\Gamma_0(F_c) = 0.03$ (below this value $\Gamma_0(F)$ begins to decrease rapidly, see Fig. 4, which is characteristic of tunneling) are $F_c = 0.11$ and 0.17 for $M = 3$ and 1836, respectively. The 1D electronic SS defined by Eq. (60) is needed to implement AAnf. The energy $\mathcal{E}_e(R, F)$ and ionization rate $\Gamma_e(R, F)$ [see Eq. (62)] of this SS calculated using the potential (86) with the parameters for $M = 1836$ at the equilibrium internuclear distance $R = R_{\rm mol}$ as functions of F are also shown in the figure. To facilitate comparison with the molecular SS results, the dashed (blue) lines in the top and bottom panels show functions $\mathrm{Re}[U_{\rm mol}(R_{\rm mol}, F)] = U_{\rm ion}(R_{\rm mol}) + \mathcal{E}_e(R_{\rm mol}, F)$ and $-2\,\mathrm{Im}[U_{\rm mol}(R_{\rm mol}, F)] = \Gamma_e(R_{\rm mol}, F)$, respectively. In the limit $M \to \infty$, for not too strong fields, the molecular SS eigenfunction becomes localized near the minimum of the real part of the BO potential $U_{\rm mol}(R, F)$ and the eigenvalue $E_0(F)$ converges to the value of the potential at this point. The minimum is located close to $R_{\rm mol}$, so $E_0(F)$ is close to $U_{\rm mol}(R_{\rm mol}, F)$. This explains why the molecular and electronic SS results for $M = 1836$ are so close to each other. All the SS energies shown in the top panel of Fig. 4 have zero slope at $F = 0$. This reflects the fact that we consider a homonuclear molecule, which does not have a permanent dipole moment, and therefore there is no linear Stark shift. The ionization rates decay exponentially as $F \to 0$ and can in this limit be described by the WFAT, as detailed in Refs. [38,40].

B. Light nuclei: AAf

Our first goal is to validate AAf by demonstrating how its results converge to TDSE results as $\epsilon_{\rm f} \to 0$. Since T_n grows as $O(M^{1/2})$ for large M and the calculation time for solving the TDSE grows rapidly with T_f, from a computational standpoint it is easier to satisfy the condition (36) for light nuclei; solving the TDSE for heavy nuclei in the region (36) is not feasible with our computational resources. Thus, in this subsection we consider the light nuclei model with $M = 3$. In this model, the electronic timescale is estimated as $T_e = 2\pi/I_p = 13.6$, where $I_p = \varepsilon_0 - E_0 = 0.464$ is the ionization potential. The nuclear timescale is $T_n = 2\pi/\Delta E_n = 19.4$, where $\Delta E_n = E_1 - E_0 = 0.324$. These timescales are comparable, which facilitates the calculations. We wish to demonstrate the convergence as T_f grows, that is, by moving to the right slightly above the lower boundary of the wedge-shaped (red) shaded region in Fig. 1.

1. Half-cycle pulses

The present version of AAf does not account for rescattering. It is possible to extend the theory to include rescattering (see Ref. [44]), but that is beyond the scope of this work. We begin with demonstrating the performance of AAf for half-cycle pulses defined by Eqs. (82) and (83). There is no rescattering in this case [44,56], so the TDSE and AAf results are expected to converge faster as $T_f = T$ grows.

The convergence is illustrated in Fig. 5. This figure shows partial PEMDs $P_v(k)$ generated by four representative half-cycle pulses. The duration of the shorter pulses $T = 30$ only slightly exceeds the nuclear timescale T_n, corresponding to the onset of the adiabatic regime (36), while that of the longer pulses $T = 150$ essentially exceeds it. The field amplitude of the weaker pulses $F_0 = 0.1 < F_c$ is just below the critical field, while that of the stronger pulses $F_0 = 0.2 > F_c$ is deep in the over-the-barrier regime of ionization. One can see

that for the shorter pulses AAf approximately describes only the partial PEMD with $v = 0$ (top lines in each panel), and in this case it works better for the stronger pulse. On the other hand, for the longer pulses the agreement between AAf and TDSE becomes quantitative for all v considered. The main conclusion to be drawn from the figure is that the AAf results converge to the TDSE results as T_f grows inside the region (36), and this holds uniformly in F for both tunneling and over-the-barrier regimes. Similar conclusions were drawn from previous applications of the adiabatic theory to atomic systems [30,44,47,51,56].

Let us discuss some additional general features of the TDSE and AAf results illustrated by Fig. 5. We begin by noting that in the *simple* asymptotics for $\epsilon_f \to 0$ developed in Sec. V A only real solutions to Eq. (55) are taken into account. Such solutions exist only in a finite interval of k defining the classical support of the PEMD [44]. For example, for the present half-cycle pulses, Eq. (55) has only one real solution in the interval $mv_\infty < k < 0$, where $v_\infty = -\frac{\sqrt{\pi}}{2}F_0T$. The AAf results for $P_v(k)$ obtained from Eq. (57) turn to zero outside this interval. The TDSE results extend beyond this interval, but the degree of the extent is seen to decrease as T_f grows. We mention that it is possible to account for the tails of $P_v(k)$ extending beyond its classical support by developing a *uniform* asymptotics for $\epsilon_f \to 0$, as was done for atomic systems in Refs. [44,56]. However, the tails become negligible for sufficiently large T_f, so even within the simple asymptotics the AAf results converge to the TDSE results.

The good performance of AAf enables us to explain some features of the TDSE results by means of Eq. (57). For example, the magnitude of the partial PEMDs $P_v(k)$ is seen to rapidly decrease as the vibrational quantum number v in the final state of the molecular ion grows. This behavior is determined by the dependence on v of the channel ionization amplitudes $f_v(F)$ defined by Eq. (39). The amplitudes describe static-field ionization of the molecule into the different vibrational channels. Their magnitude depends exponentially on the energy difference $\varepsilon_v - E_0$, as can be seen from the field factor in the WFAT [38,39,42]. For the present case of light nuclei, this difference grows rapidly with v, which explains the rapid decrease of $f_v(F)$, and hence $P_v(k)$. Another notable feature in Fig. 5 is the asymmetry of the distributions $P_v(k)$. The right shoulders of the distributions are suppressed compared to their left shoulders, and this becomes more pronounced for stronger and longer pulses. This is caused by depletion described by the imaginary part of the term $s_0(t_i)$ in the exponent in Eq. (57). Indeed, Eq. (55) establishes a mapping between ionization time t_i and momentum k. For half-cycle pulses, smaller $|k|$ correspond to larger t_i. The imaginary part of $s_0(t_i)$ is negative and grows with t_i, see Eqs. (42) and (48), which causes the suppression of $P_v(k)$ at smaller $|k|$.

To quantify the depletion, we consider the probability for the molecule to remain in the initial ground state after the end of the pulse. The results calculated for the same pulses as in Fig. 5 are presented in Table I. Only a tiny fraction of the initial state survives the interaction with the longest and strongest pulse, and this is reflected in the strong asymmetry of the PEMDs in the bottom right panel in Fig. 5. The AAf results are again seen to converge to the TDSE results as T_f grows, which supports the above conclusion.

TABLE I. Probabilities for the molecule to survive in the initial ground state for the same model and pulses as in Fig. 5. The TDSE results P_0 are obtained from Eq. (10) and the AAf results $P_0^{\rm f}$ are obtained from Eq. (52).

	$T = 30$		$T = 150$	
	$F_0 = 0.1$	$F_0 = 0.2$	$F_0 = 0.1$	$F_0 = 0.2$
P_0	0.630	0.00492	0.309	1.43×10^{-8}
$P_0^{\rm f}$	0.796	0.02803	0.320	1.73×10^{-8}

One more feature worth mentioning here is the series of sharp peaks seen in Fig. 5 in the TDSE results for the shorter pulses around $k = 0$. These peaks originate from Feshbach resonances in electron scattering by the molecular ion; they are also seen in the scattering matrix defined by Eqs. (6). Similar peaks originating from shape resonances in electron-ion scattering were seen in PEMDs for atomic systems [44]. They are caused by direct excitation of resonance states of the target system by the laser pulse. Such nonadiabatic transitions are not accounted for by the present theory, because their probability exponentially decays as T_f grows.

2. *Few-cycle pulses*

We next illustrate the performance of AAf for more realistic few-cycle pulses defined by Eqs. (82) and (84). The main novel feature in this case is the appearance of rescattering [44,56]. We consider two-cycle pulses with $n_{\rm oc} = 2$, so the field timescale is $T_f = T/4$. Figure 6 shows partial PEMDs $P_v(k)$ generated by two such pulses with the amplitude $F_0 = 0.1$ in the tunneling regime of ionization and durations $T = 250$ and 500. Figure 7 presents similar results for pulses with the over-the-barrier amplitude $F_0 = 0.2$ and durations $T = 150$ and 300.

Let us first consider the results for the weaker pulses shown in Fig. 6. The agreement between AAf and TDSE results for the partial PEMD with $v = 0$ essentially improves as T is increased. Note that for the longer pulse $T_f = 125$, which is slightly smaller than the value of T_f in the top right panel in Fig. 5. The remaining difference between the results is localized at large $|k|$, where the TDSE results extend beyond the classical support of the PEMD, and small $|k|$, which is caused by rescattering. The agreement is expected to further improve at larger T; however, solving the TDSE for larger T is not feasible with our computational resources. The difference between AAf and TDSE results for partial PEMDs with $v > 0$ is more significant. This is explained as follows. The present version of AAf without rescattering accounts only for the direct strong-field ionization of the initial bound state. The dependence of the magnitudes of $P_v(k)$ on v in this approximation is determined by the channel ionization amplitudes $f_v(F)$ which rapidly decay as v grows, as explained in the previous subsection. This decay is seen in the AAf results. Meanwhile, inelastic rescattering processes change the vibrational state of the parent molecular ion, which results in populating states with larger v. This modifies the distribution of partial PEMDs

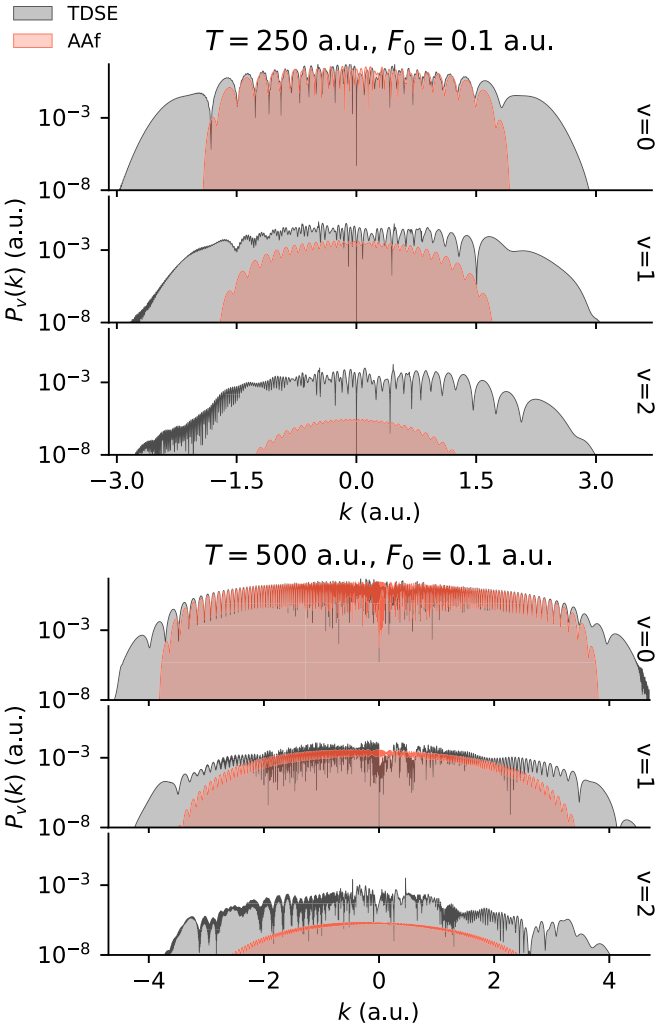

FIG. 6. Partial PEMDs $P_v(k)$ for the light nuclei model ($M = 3$) generated by two-cycle ($n_{oc} = 2$) pulses with the amplitude $F_0 = 0.1$ and durations T indicated in the figure. The TDSE results (darker lines) are obtained from Eq. (12) and the AAf results (lighter lines) are calculated using Eq. (57).

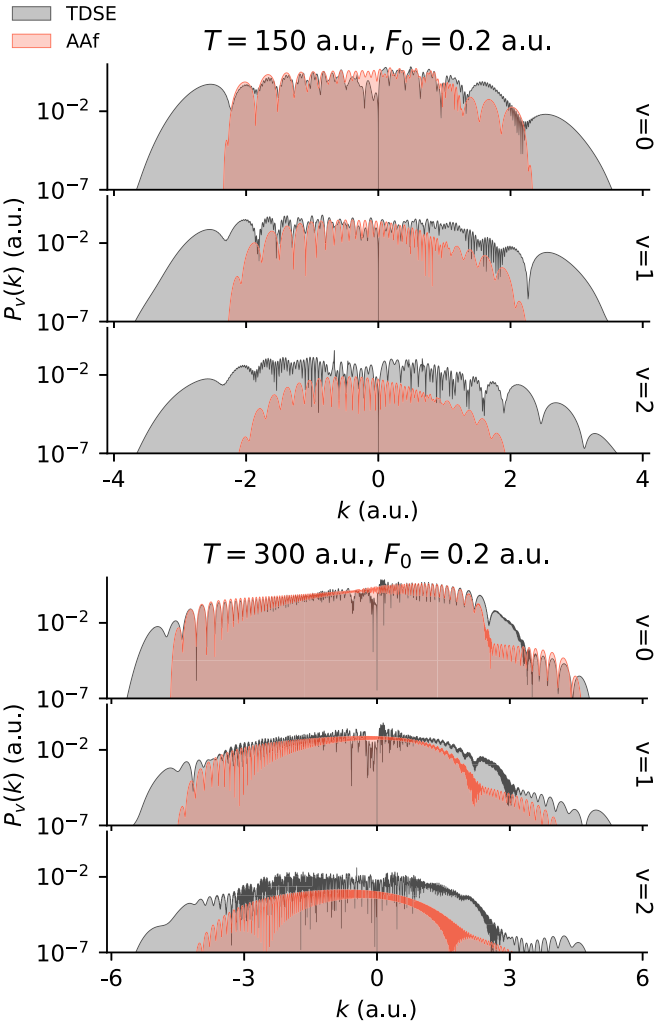

FIG. 7. Same as in Fig. 6, but for the pulse amplitude $F_0 = 0.2$.

over v, leading to an increase of $P_v(k)$ for larger v. Indeed, the TDSE results in Fig. 6 decay much more slowly in v than in the case of half-cycle pulses; compare with Fig. 5. We note that even for PEMDs with $v > 0$ the difference between AAf and TDSE results decreases as T is increased. This is because the second term in Eq. (46) is $O(\epsilon_f^{1/2})$, so the relative role of rescattering processes decreases as $\epsilon_f \to 0$. Thus, the AAf and TDSE results for $v > 0$ should also converge as T grows, although we cannot illustrate this numerically.

The situation with the results for the stronger pulses shown in Fig. 7 is similar. All the above arguments apply in this case as well. An interesting feature to be noted is that the convergence of the AAf and TDSE results for $v > 0$ as T grows is faster. This observation suggests that for stronger fields the relative role of rescattering decreases. Summarizing, we conclude that for few-cycle pulses the AAf results also converge to the TDSE results in the region (36), both in the tunneling and over-the-barrier regimes of ionization, although the convergence is slower than for half-cycle pulses because of rescattering processes not accounted for by the present version of AAf.

The main visible difference of the PEMDs shown in Figs. 6 and 7 from those in Fig. 5 is the appearance of a prominent oscillatory structure. This structure can be explained within AAf. For few-cycle pulses, Eq. (55) has several solutions contributing to the ionization amplitude (57). The oscillations of $P_v(k)$ result from the interference of the different terms in Eq. (57). For half-cycle pulses, there is only one term, so there is no interference. From a careful inspection of Figs. 6 and 7, one can observe that the interference structure of the AAf results also appears in the TDSE results, but in addition the TDSE results contain a more rapidly oscillating substructure not reproduced by AAf. This substructure originates from the interference of the direct and rescattering contributions to the PEMD. Its contrast thus reflects the relative role of the contributions. For example, in the top panel of Fig. 6, rescattering is weak for $v = 0$, so the oscillations in the TDSE results follow that in the AAf results and the more rapidly oscillating substructure has a small amplitude. On the other hand, for $v = 1$ in the region $-1.5 < k < 0$, direct and rescattering contributions are comparable, so the amplitude of the substructure is larger. For $v = 2$ in the same panel, the direct

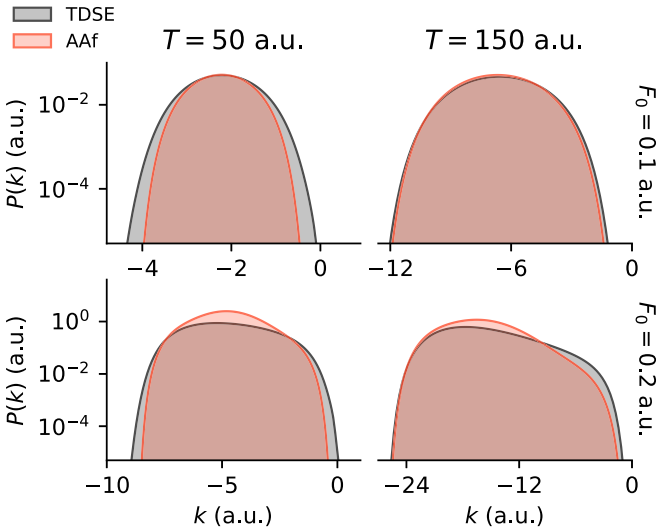

FIG. 8. Total PEMD $P(k)$ for the heavy nuclei model ($M = 1836$) generated by half-cycle pulses with amplitudes F_0 and durations T indicated in the figure. The TDSE results (darker lines) are obtained from Eq. (14) and the AAf results (lighter lines) are calculated using Eq. (57).

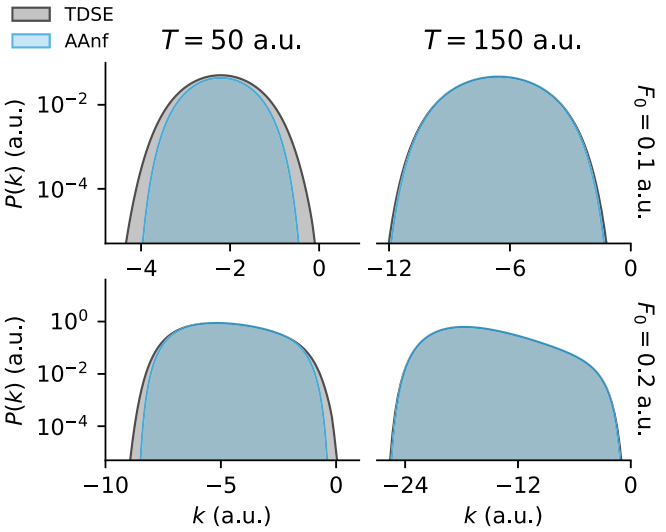

FIG. 9. Same as in Fig. 8, but with the AAf results replaced by the AAnf results calculated using Eq. (73).

contribution represented by the AAf results is very weak, so the substructure is probably caused by the interference of the different rescattering trajectories [44,56].

C. Heavy nuclei: AAnf

The goal of this subsection is to validate AAnf. TDSE calculations in the region (58) are feasible in a wide range of the nuclear mass. We therefore consider here the more realistic heavy nuclei model with $M = 1836$. In this model, the electronic and nuclear timescales estimated as above are $T_e = 11.1$ and $T_n = 288$, so the condition $T_e \ll T_n$ is well satisfied. We validate AAnf by demonstrating the convergence of its results to the TDSE results as T_f grows. This corresponds to moving to the right along the lower dashed line indicated by H_2 in Fig. 1 deeper inside the rectangular (blue) shaded region.

1. Half-cycle pulses

To exclude rescattering, we again begin with half-cycle pulses defined by Eqs. (82) and (83), as in Sec. VI B 1. We consider pulses with two amplitudes, weaker pulses with $F_0 = 0.1 < F_c$ in the tunneling regime and stronger pulses with $F_0 = 0.2 > F_c$ in the over-the-barrier regime. For each amplitude, we have performed calculations for two pulse durations $T = 50$ and 150. Although our main goal here is to demonstrate the convergence of AAnf, it is also instructive to see the breakdown of AAf outside the region (36). In this subsection, we compare the performance of AAf and AAnf for the same half-cycle pulses.

The comparison of the AAf and AAnf results with the TDSE results is presented in Figs. 8 and 9, respectively. For the present heavy nuclei model, the energy spacing between vibrational states of the molecular ion becomes quite small (compare Figs. 2 and 3), so many different v channels contribute comparably to the total ionization yield. Since it is not practical to plot many partial PEMDs, in Figs. 8 and 9 we show only the total PEMD $P(k)$ defined by Eq. (14). For the weaker pulses in Fig. 8, the AAf results seem to give a reasonable approximation to the TDSE results. However, for the stronger pulses, the agreement clearly becomes worse. This is not surprising, because in the present case $T_n > T_f$ even for the longest pulses considered. The condition (36) does not hold and hence AAf fails. On the other hand, Fig. 9 shows that the AAnf results converge to the TDSE results as T grows, and the convergence for the stronger pulses is faster. For the longer pulses, the agreement is almost perfect, and this holds in both tunneling and over-the-barrier regimes of ionization.

We continue the comparison by looking at the distribution of channel ionization probabilities $P_v^{\rm ion}$ defined by Eq. (13). The results for the same pulses as in Figs. 8 and 9 are shown in Fig. 10. The TDSE results confirm the above assertion that many different vibrational channels contribute to the total ionization yield in the heavy nuclei case. Moreover, in contrast to the light nuclei case, the channel with $v = 0$ is now not even the dominant one; the distributions are seen to peak around $v = 2$. The AAf results demonstrate some improvement as T grows for the weaker pulses, but are rather far from the TDSE results for the stronger pulses. On the other hand, the AAnf results converge to the TDSE results for both field strengths considered, and for the stronger pulses the convergence is faster.

Let us now briefly look at partial PEMDs. We consider only one pulse with $T = 150$ and $F_0 = 0.2$, for which the AAnf results in Figs. 9 and 10 almost perfectly agree with the TDSE results. The different results for a few partial PEMDs $P_v(k)$ generated by this pulse are compared in Fig. 11. The figure shows that even this fully differential ionization observable is very well reproduced by AAnf, while AAf fails similarly to how it fails for the total PEMD in the bottom right panel in Fig. 8.

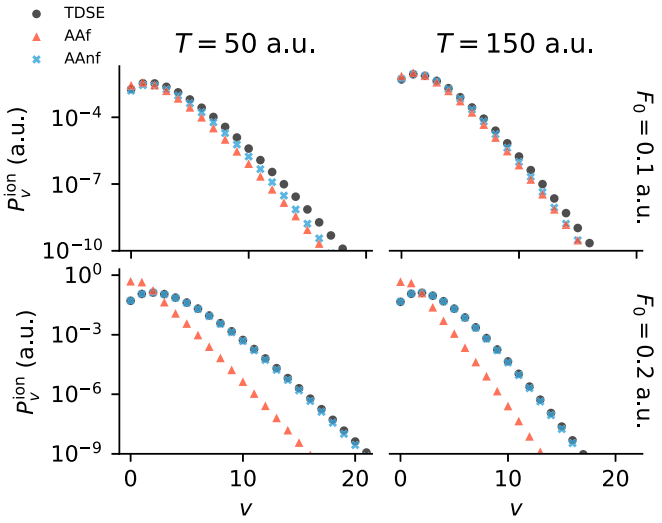

FIG. 10. Channel ionization probabilities $P_v^{\rm ion}$ for the same model and pulses as in Figs. 8 and 9. The TDSE results (circles) are obtained from Eq. (13), the AAf results (triangles) are calculated using Eq. (57), and the AAnf (crosses) results are calculated using Eq. (73).

The last feature we wish to discuss for half-cycle pulses is the distribution of probabilities P_n that the molecule survives in a bound state after the end of the pulse. The results for the same four pulses as in Figs. 8, 9, and 10 are shown in Fig. 12. Here we show only the TDSE and AAnf results, because AAf does not account for transitions to excited states with $n > 0$. In the TDSE results, a distinction is made between bound states that are even and odd in x. As mentioned above, in the BOA even and odd molecular states correspond to the

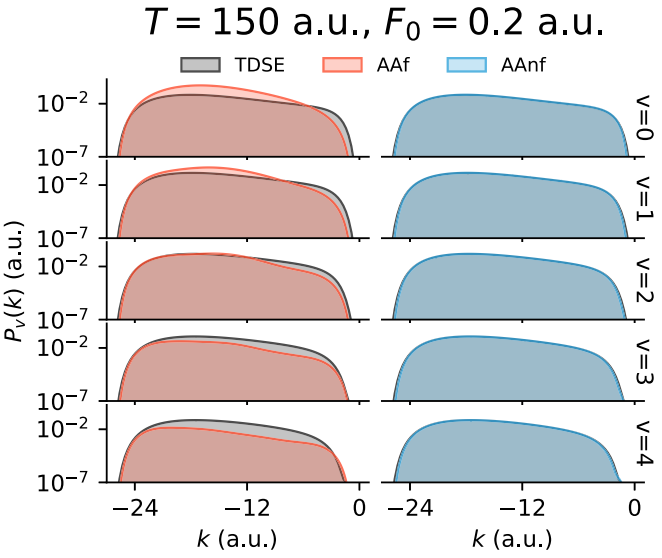

FIG. 11. Partial PEMDs $P_v(k)$ for the same model and pulse as in the bottom right panel in Figs. 8, 9, and 10. The TDSE results (darker lines in both left and right panels) are obtained from Eq. (12), the AAf results (lighter lines in the left panels) are calculated using Eq. (57), and the AAnf results (lighter lines in the right panels, almost indistinguishable from the TDSE results) are calculated using Eq. (73).

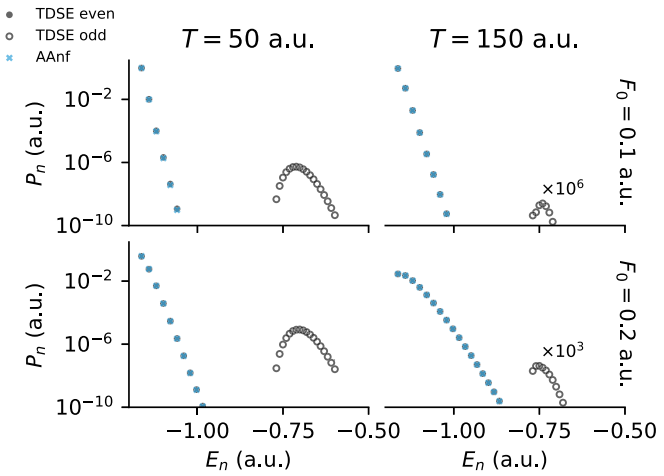

FIG. 12. Probabilities P_n that the molecule survives in a bound state as functions of the energy E_n of the state for the same model and pulses as in Figs. 8, 9, and 10. The solid (open) circles show the TDSE results obtained from Eq. (10) for bound states with even (odd) symmetry in x, corresponding to the ground (first excited) electronic state within the BOA. In the right panels, the TDSE results for the odd states are multiplied by a factor indicated in the figure. The crosses show the AAnf results for the even states obtained from Eq. (71).

ground and first exited electronic states and are supported by the lowest (black) and intermediate (blue) BO potentials in Fig. 3, respectively. One can see that the population of the even states monotonically decays as the energy of the state grows, while that of the odd states has a peak at some intermediate vibrational state in the electronically excited potential. Furthermore, probabilities of transitions to odd states rapidly decay as T grows (notice the factors multiplying the probabilities in the right panels), because such transitions involve excitation of the electron and are suppressed for $T_e \ll T_f$. The present AAnf only describes transitions to even states. For all pulses considered, the AAnf results are on top of the TDSE results for the even states, which additionally confirms the good performance of AAnf.

Summarizing, we have shown that for a realistic nuclear mass the AAnf results converge to the TDSE results as T_f grows. This validates AAnf in the region (58). For the heavy nuclei model and pulses considered here, we have $T_f < T_n$, so the condition (36) is not satisfied, which explains the failure of AAf.

2. *Compatibility of* AAf *and* AAnf

As T_f is further increased for the same model, which corresponds to moving to the right along the dashed line indicated by H_2 in Fig. 1, we eventually enter the region (36). In this region, AAf is expected to work well. It is, however, not possible for us to check this directly by performing TDSE calculations for heavy nuclei at $T_f \gg T_n$. Meanwhile, AAf and AAnf can be easily implemented at any T_f. Since we have already seen that the AAnf results converge to the TDSE results, we can validate AAf for heavy nuclei indirectly by demonstrating the convergence of its results to the AAnf results. For completeness of the presentation, we believe it is

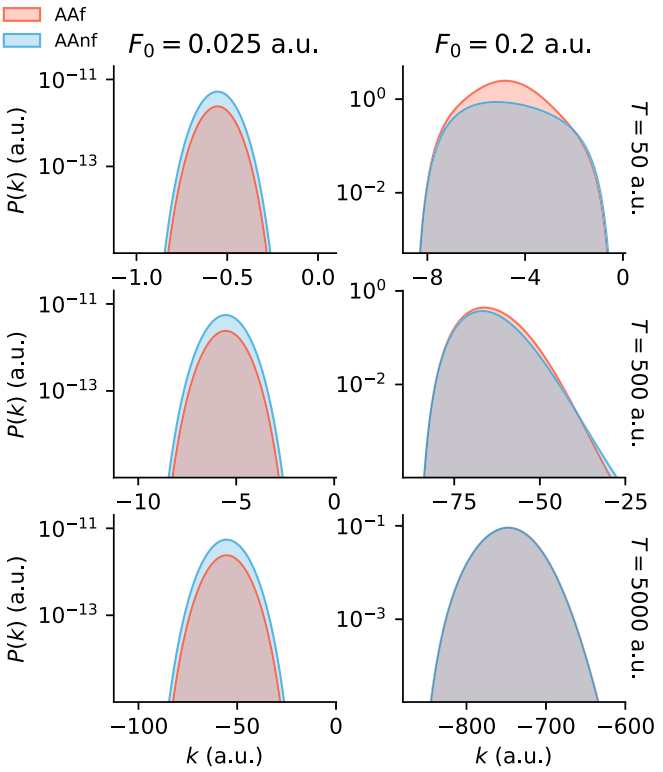

FIG. 13. Total PEMD $P(k)$ for the heavy nuclei model ($M = 1836$) generated by half-cycle pulses with amplitudes F_0 and durations T indicated in the figure. The AAf (lower lines in the left panels and upper lines in the right panels) and AAnf results are calculated using Eqs. (57) and (73), respectively.

instructive to demonstrate compatibility of the two adiabatic approximations at very large T_f, in the region where they both apply.

We again consider half-cycle pulses with two amplitudes and growing durations. The stronger pulses have the same amplitude $F_0 = 0.2$ as in the previous subsection, but the amplitude of the weaker pulses $F_0 = 0.025$ is chosen four times smaller than that in the previous subsection. The comparison of the AAf and AAnf results is presented in Fig. 13. One can see that for the stronger pulses the AAf and AAnf results indeed converge as T grows. However, this is not the case for the weaker pulses. The reason for this is the breakdown of the BOA, on which AAnf is based, in describing tunneling ionization at sufficiently weak fields [38]. As was mentioned in the end of Sec. V C, the breakdown occurs at fields $F_0 \lesssim F_{\rm BO}$, where for the present system $F_{\rm BO} = 0.048$. Thus, the BO approximation breaks down, and hence AAnf is not applicable, for the weaker pulses. Note, importantly, that the situation cannot be improved by increasing T_f. On the other hand, the convergence of AAf is uniform in F_0, that is, it can be achieved for any F_0 at sufficiently large T_f. We conclude that the AAf results for the weaker and longer pulses in Fig. 13 are expected to be more accurate than AAnf.

3. *Few-cycle pulses*

We complete the validation of AAnf by considering few-cycle pulses defined by Eqs. (82) and (84) with $n_{\rm oc} = 2$, as in Sec. VI B 2. We have performed calculations for pulses with the amplitudes $F_0 = 0.1$ and 0.2 and durations $T = 200$ and 320 corresponding to $T_f = 50$ and 80, respectively. Figure 14 compares the TDSE and AAnf results for the total PEMD $P(k)$. The results converge as T grows and for the longer pulses a good agreement over a wide interval of k is achieved. Notice that there remains some disagreement at small $|k|$, which is caused by rescattering, and at large $|k|$, where the TDSE results extend beyond the classical support of the PEMD. The origin of this disagreement was discussed in Sec. VI B 2.

Figure 15 presents the corresponding results for the distribution of channel ionization probabilities $P_v^{\rm ion}$ defined by Eq. (13). The agreement between the AAnf and TDSE results

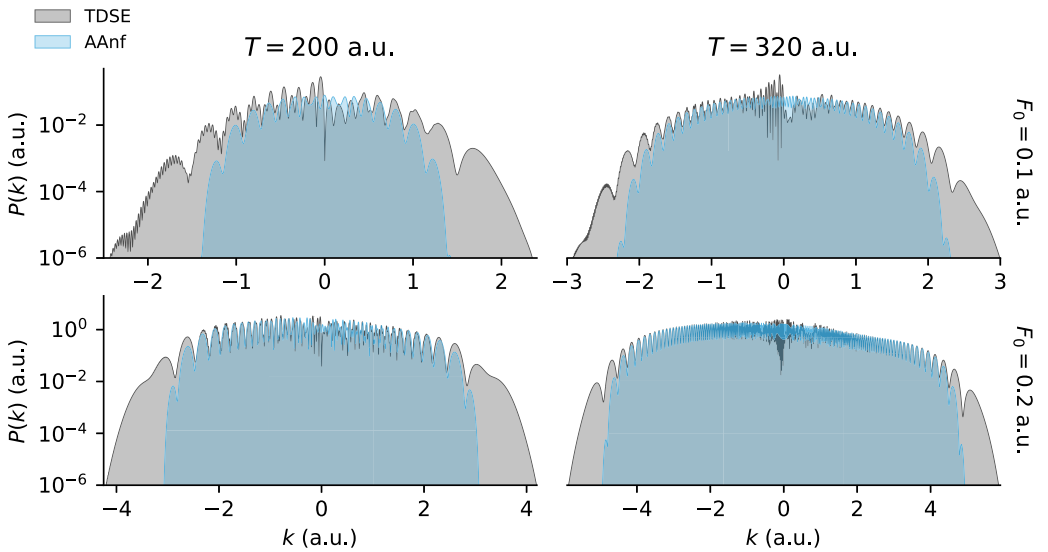

FIG. 14. Total PEMD $P(k)$ for the heavy nuclei model ($M = 1836$) generated by two-cycle ($n_{\rm oc} = 2$) pulses with the amplitudes and durations indicated in the figure. The TDSE results (darker lines) are obtained from Eq. (14) and the AAnf results (lighter lines) are calculated using Eq. (73).

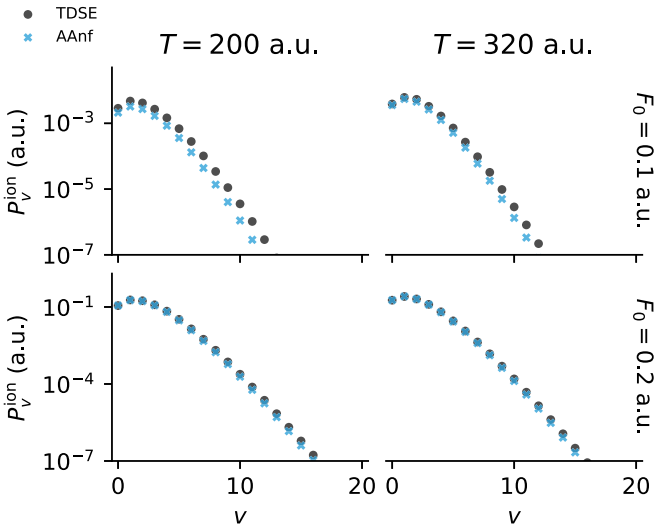

FIG. 15. Channel ionization probabilities $P_v^{\rm ion}$ for the same model and pulses as in Fig. 14. The TDSE results (circles) are obtained from Eq. (13) and the AAnf results (crosses) are calculated using Eq. (73).

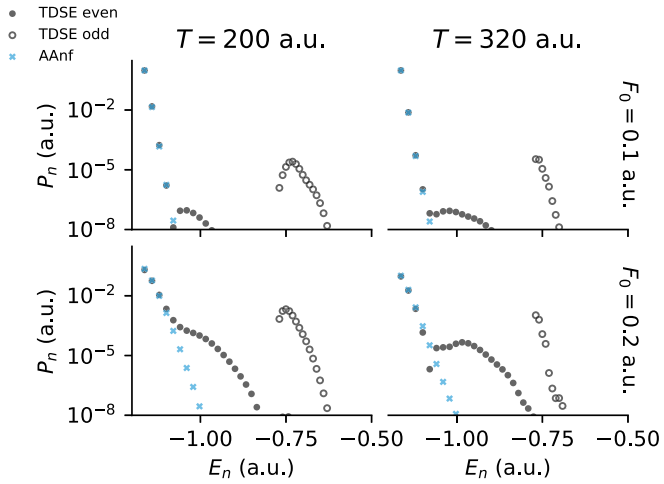

FIG. 17. Probabilities P_n that the molecule survives in a bound state as functions of the energy E_n of the state for the same model and pulses as in Figs. 14 and 15. The solid (open) circles show the TDSE results obtained from Eq. (10) for states with even (odd) symmetry in x. The crosses show the AAnf results for the even states obtained from Eq. (71).

is seen to be quite good and improves for the longer pulses. In addition, the convergence for the stronger pulses is faster, which is also the case for the results shown in Fig. 14.

Figure 16 compares the TDSE and AAnf results for partial PEMDs $P_v(k)$ generated by the pulse with $T = 320$ and $F_0 = 0.2$. Similar to Fig. 14, we see good agreement over a wide interval of k. Note that the agreement is good also for the higher v channels considered, which is in contrast to the situation with AAf illustrated in Figs. 6 and 7. This suggests that rescattering plays a smaller role for heavy nuclei. One more feature to be observed in Fig. 16 is that the interference

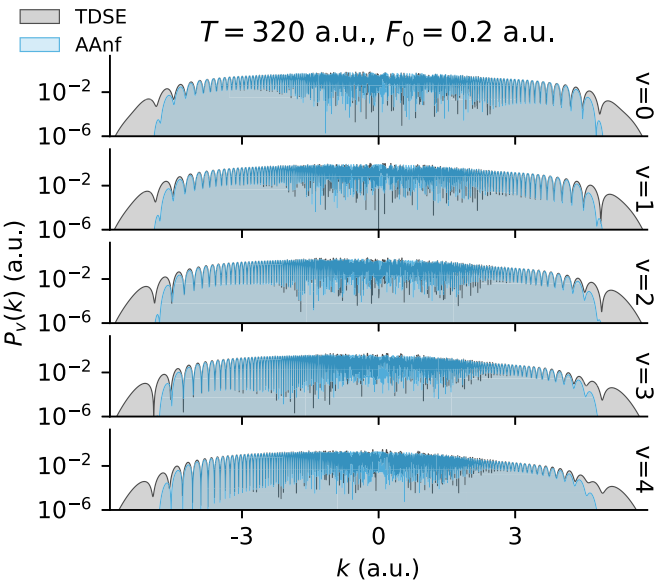

FIG. 16. Partial PEMDs $P_v(k)$ for the same model and pulse as in the bottom right panel in Figs. 14 and 15. The TDSE results (darker lines) are obtained from Eq. (12) and the AAnf results (lighter lines) are calculated using Eq. (73).

structure in all the partial PEMDs has the same phase. This structure is mainly determined by the difference between classical actions in the exponent for the different terms in the sum over i in Eq. (73). This action depends only on the final momentum k and not on the vibrational channel index v, which explains the observation. The same applies to AAf, as can be seen from Eq. (57).

Finally, we show in Fig. 17 the distribution of probabilities P_n for the molecule to survive in a bound state. These results should be compared to Fig. 12. AAnf is seen to work well for several lowest even states. However, it fails for the higher even states. The drastic change in the behavior of the TDSE results in this case is probably caused by excitation processes not accounted for by AAnf, which become more efficient and selective for few-cycle pulses. The excitation of even states occurs through an intermediate odd state. Indeed, we see that the final populations of odd states have grown considerably compared to that for half-cycle pulses. We note that rescattering may also play a role in the failure of AAnf for the higher states.

VII. ILLUSTRATIVE CALCULATIONS: APPLICATIONS

In this section, we present two examples illustrating the usefulness of the adiabatic theory for applications in strong-field physics. To stay closer to reality, here we consider molecules with heavy nuclei and pulses with the frequency $\omega = 0.057$ corresponding to the wavelength 800 nm. The corresponding timescales belong to the region (58), but are outside the region (36). We therefore base our analysis on AAnf. The first example shows how AAnf can be used to treat pulses for which solving the TDSE is not feasible. The second example illustrates how AAnf can help in explaining differences in observables for molecules consisting of different isotopes.

A. Interference structures in partial photoelectron momentum distributions

Here we discuss interference structures in the partial PEMDs $P_v(k)$ generated by multicycle almost monochromatic pulses described by Eqs. (82) and (84) with fixed ω and $n_{\rm oc} \to \infty$. The computational time required to solve the TDSE with our program grows rapidly with $n_{\rm oc}$ (see the Appendix). We mention that it grows even faster as ω is decreased while keeping $n_{\rm oc}$ fixed. In such situations, especially for strong fields, solving the TDSE quickly becomes unfeasible. At the same time, AAnf can be implemented almost with the same ease for any $n_{\rm oc}$ and ω.

For monochromatic pulses, Eq. (55) has two solutions within each optical cycle. All the solutions to Eq. (55) can be presented in the form $t_{1j} = t_1 + jT_\omega$ or $t_{2j} = t_2 + jT_\omega$, where j is an integer, $T_\omega = 2\pi/\omega$ is the laser period, and $t_1 < t_2$ denote two solutions in the interval $0 < t < T_\omega$. We can rearrange the sum over i in Eq. (73) by first summing the contributions from t_1 and t_2, and then summing the result over j enumerating optical cycles. Consider the dependence of the different terms on t_i. The solution to Eq. (66) in the monochromatic case has the Floquet form $\Psi(R,t) = \Phi(R,t)e^{-iE^{\rm BO}(F_0,\omega)t}$, where $\Phi(R,t)$ is a periodic function of t and $E^{\rm BO}(F_0,\omega)$ is the Floquet energy of the molecule in the BOA. Then one can see that the contributions from t_i and $t_i + T_\omega$ differ by a factor $e^{i\Delta\phi_{\rm inter}}$, with the *intercycle* interference phase given by

$$\Delta\phi_{\rm inter} = \Delta E T_\omega, \tag{88}$$

where

$$\Delta E = \frac{k^2}{2} + U_p + \varepsilon_v - E^{\rm BO}(F_0,\omega) \tag{89}$$

and $U_p = F_0^2/4\omega^2$ is the ponderomotive energy. On the other hand, the phase difference between the contributions from t_1 and t_2, defining the *intracycle* interference phase, is

$$\Delta\phi_{\rm intra} = \Delta E\,\Delta t - \frac{3|k|}{2\omega}\sqrt{4U_p - k^2} + \delta, \tag{90}$$

where $\Delta t = t_2 - t_1 = (\pi - 2\arcsin\frac{\omega|k|}{F_0})/\omega$ and the term δ originates from the phase of the ionization amplitude $f(R,F(t))$ and Floquet eigenfunction $\Phi(R,t)$ in Eq. (74). Thus, we expect the appearance of two interference structures in the partial PEMDs, intercycle and intracycle, defined by the phases (88) and (90), respectively.

To demonstrate this, we have performed AAnf calculations for the heavy nuclei model with $M = 1836$ for a multicycle pulse with $n_{\rm oc} = 19$. The calculation of the Floquet energy $E^{\rm BO}(F_0,\omega)$ and eigenfunction $\Phi(R,t)$ is a separate issue which goes beyond the scope of this paper. For the present illustrative purposes, we consider a rather weak pulse with $F_0 = 0.05$, for which they can be approximated by the unperturbed energy $E_0^{\rm BO}$ of the molecule and the nuclear wave function $\Psi_0(R)$ in the BOA. The phase of $f(R,F)$ in this case does not depend on F, as follows from the WFAT [39], so we set $\delta = 0$. The results are presented in Fig. 18. The solid (blue) lines in the top panel show the partial PEMDs $P_v^{\rm nf}(k)$ for the first three vibrational states as functions of the total energy $k^2/2 + \varepsilon_v$ of the ionized molecule. The vertical (gray) lines indicate the energies where the following condition for constructive intercycle interference is fulfilled:

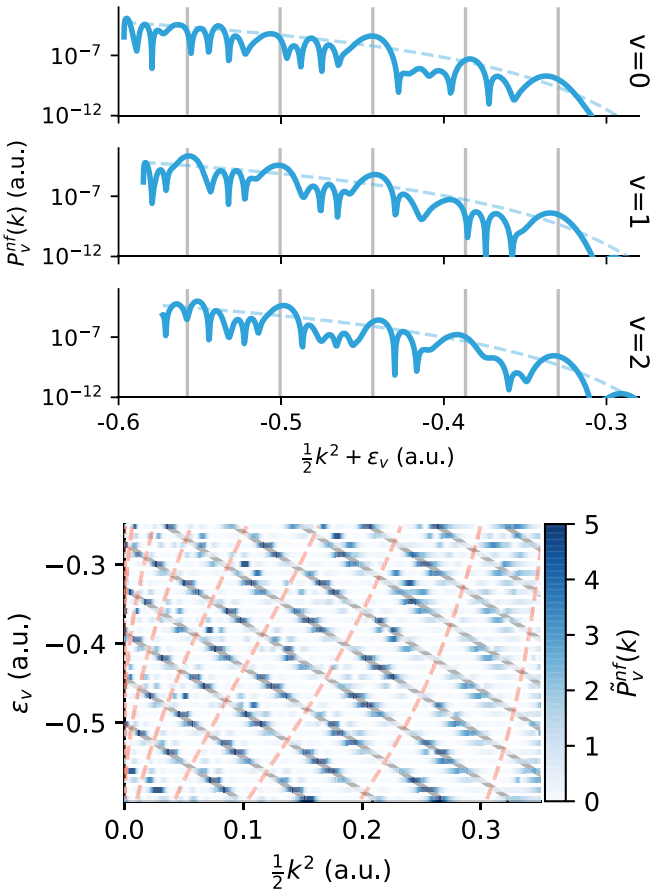

FIG. 18. Partial AAnf PEMDs for the heavy nuclei model with $M = 1836$ generated by a pulse with $\omega = 0.057$, $n_{\rm oc} = 19$, and $F_0 = 0.05$ calculated using Eq. (73). In the top panel, the solid (blue) lines show the PEMDs $P_v^{\rm nf}(k)$ as functions of $k^2/2 + \varepsilon_v$. The dashed lines show the corresponding averaged PEMDs defined by Eq. (92). The vertical (gray) lines indicate the energies where the condition (91) is fulfilled. The bottom panel shows the ratio (93) in the plane of the electronic $k^2/2$ and molecular ion ε_v energies. The conditions (91) and (94) are fulfilled along the solid (gray) lines and dashed (red) lines in this panel, respectively. The results include only electrons ejected in the positive direction $k > 0$. For multicycle pulses, the $k < 0$ results are practically identical.

$$\Delta\phi_{\rm inter} = 2\pi n, \quad n = 0, \pm 1, \ldots. \tag{91}$$

Indeed, these lines are located near the maxima of $P_v^{\rm nf}(k)$. Such maxima are counterparts of above-thresholds ionization peaks for atomic targets [65]. The intercycle interference in the joint electronic and nuclear energy spectrum for molecular targets was discussed in Ref. [15]. The corresponding interference phase given there coincides with Eq. (88) with the Floquet energy in Eq. (89) substituted by the unperturbed molecular energy. In the top panel in Fig. 18, we have additionally plotted by dashed (blue) lines averaged partial PEMDs obtained from Eq. (73) as the incoherent sum

$$\bar{P}_v^{\rm nf}(k) = 2\pi \sum_i \frac{|g_v(t_i)|^2}{|F(t_i)|}. \tag{92}$$

The bottom panel shows the ratios

$$\tilde{P}_v^{\rm nf}(k) = \frac{P_v^{\rm nf}(k)}{\bar{P}_v^{\rm nf}(k)}, \tag{93}$$

which emphasize the interference structures. The solid (gray) lines connect points in the plane of the electronic $k^2/2$ and molecular ion ε_v energies where the condition (91) is fulfilled. The fact that these lines pass through the maxima of the $P_v^{\rm nf}(k)$ is more clearly seen now. The dashed (red) lines indicate points where the condition for destructive intracycle interference is fulfilled

$$\Delta\phi_{\rm intra} = \pi(2n+1), \quad n = 0, \pm 1, \ldots. \tag{94}$$

These lines closely reproduce minima of $P_v^{\rm nf}(k)$ extending in a direction almost perpendicular to the intercycle maximum lines. The intracycle interference in dissociative ionization of molecules was discussed in Ref. [66]. The corresponding interference phase given there coincides with Eq. (90), with the Floquet energy in Eq. (89) again substituted by the unperturbed molecular energy, as in Ref. [15], and the term δ omitted. Note that although we have also used these approximations in the present illustrative calculations, the exact intercycle (88) and intracycle (90) interference phases obtained within AAnf differ from that in Refs. [15] and [66].

B. Isotope effect

We now use AAnf to discuss the isotope effect in molecular strong-field observables. Here, we consider channel ionization probabilities $P_v^{\rm ion}$. We have performed TDSE calculations for the heavy nuclei model (see Sec. VI A) with nuclear masses $M = m_p$, $2m_p$, and $4m_p$, where $m_p = 1836$ is the proton mass, for a few-cycle pulse with $n_{\rm oc} = 2$ and $F_0 = 0.15$. The results are presented by solid circles in Fig. 19. One can see a strong isotope effect in the distribution of $P_v^{\rm ion}$ as a function of the ionic energy ε_v: As the nuclear mass grows, the distribution becomes narrower. We mention that there is no strong mass dependence in the shape of the partial PEMDs $P_v(k)$ as functions of k, that is why we consider channel ionization probabilities [see Eq. (13)]. For the largest nuclear mass considered, $M = 4m_p$, we also show AAnf results. These are seen to be quite close to the corresponding TDSE results. This enables us to explain the isotope effect by means of Eq. (73).

The main dependence of the ionization amplitude (73) on ε_v comes from the factor (74). In the limit $M \to \infty$, this factor can be evaluated using the reflection approximation. This approximation amounts to replacing the ionic state $\chi_v(R)$ in the integrand by a function proportional to $\delta(R - R_v)$, where $R_v < R_{\rm ion}$ is the inner turning point defined by $U_{\rm ion}(R_v) = \varepsilon_v$ [64]. Then the result for $g_v(t)$ is proportional to $\Psi(R_v, t)$. For fields that are not too strong, this function can be approximated by the unperturbed solution (70) to Eq. (66), which gives $P_v^{\rm nf}(k) \propto |\Psi_0(R_v)|^2$. Since the nuclear wave function $\Psi_0(R)$ for $M \to \infty$ is localized near $R = R_{\rm mol}$, we expect that the probability density $|\Psi_0(R_v)|^2$ represents the main dependence of $P_v^{\rm nf}(k)$, and hence $P_v^{\rm ion}$, on ε_v. This density for $M = 4m_p$, normalized to the maximum of the corresponding distribution $P_v^{\rm ion}$, is plotted by the solid line in Fig. 19. In view of the approximations made, we did not expect that it would closely reproduce the TDSE and AAnf results. However, it does approximately reproduce the overall shape of the results. The agreement could be improved by including the ionization amplitude $f(R, F)$ factor from Eq. (74); we do not discuss this because the AAnf results obtained by implementing Eq. (73) without any approximations are already shown to agree well with the TDSE results. The width of $|\Psi_0(R_v)|^2$ decreases as M grows, which explains the decrease of the width of the distribution of $P_v^{\rm ion}$ seen in Fig. 19. In Ref. [35], distributions of $P_v^{\rm ion}$ for the real H_2 molecule produced by intense laser pulses were measured experimentally. Our theory and calculations predict that similar distributions for D_2 would be narrower.

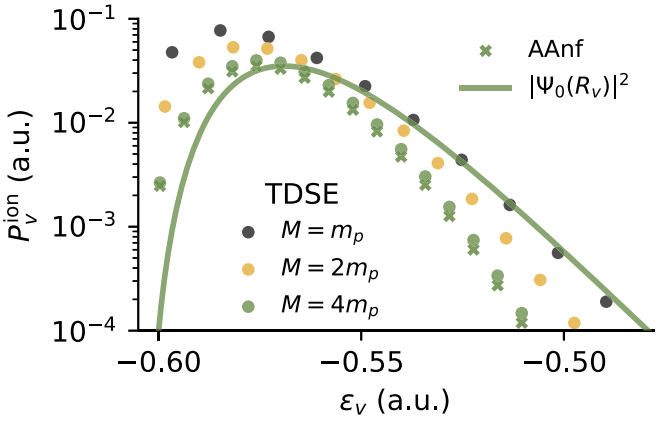

FIG. 19. Solid circles show the TDSE results for the channel ionization probabilities $P_v^{\rm ion}$ for the heavy nuclei model with $M = m_p$, $2m_p$, and $4m_p$ (from top to bottom), where $m_p = 1836$, obtained from Eq. (13) for a few-cycle pulse with $\omega = 0.057$, $n_{\rm oc} = 2$, and $F_0 = 0.15$. The results are shown as functions of the ionic energy ε_v. Crosses show the corresponding AAnf results for the largest nuclear mass $M = 4m_p$ calculated using Eq. (73). The solid line shows the unperturbed ground-state nuclear probability density $|\Psi_0(R_v)|^2$ for $M = 4m_p$, where the ionic turning point R_v is a function of ε_v defined by $U_{\rm ion}(R_v) = \varepsilon_v$. The solid line is normalized to the AAnf results at the maximum.

In Ref. [36], the dependence of the total ionization rate in a static electric field on the nuclear mass for isotopes of molecular hydrogen was predicted based on the WFAT [39]. The rate was shown to decrease as the the nuclear mass grows. This prediction was confirmed experimentally by measuring the ratio of total ionization yields for H_2 and D_2 produced by circular polarized laser pluses at 800-nm wavelength [37]. Here we can address the question of whether the prediction of Ref. [36] for ionization *rates* in a static field holds for ionization *yields* in a time-dependent laser field measured in Ref. [37]. The total ionization probabilities [see Eq. (15)] in the calculations discussed above are $P_{\rm ion} = 0.275$, 0.257, and 0.241 for $M = m_p$, $2m_p$, and $4m_p$, respectively. Thus $P_{\rm ion}$ indeed decreases as M grows, in agreement with Ref. [36].

VIII. CONCLUSIONS AND OUTLOOK

We have developed the adiabatic theory of ionization of molecules by intense laser pulses with the internuclear motion taken into account. The structure of the theory depends on the relation between electronic T_e, nuclear T_n, and laser field T_f timescales. We have considered two regimes that are most

relevant for applications in strong-field physics: field is the slowest, Eq. (36), and electron is the fastest, Eq. (58). The corresponding versions of the adiabatic theory are denoted by AAf and AAnf, respectively. The adiabatic asymptotics of the ionization amplitude (11) defining all the ionization observables within AAf and AAnf are given by Eqs. (57) and (73), respectively. These formulas present the main results of this paper. The compatibility of AAf and AAnf in the overlap region (75) where the two adiabatic approximations apply simultaneously is shown. The theories are validated by comparing their predictions with TDSE calculations for a model diatomic molecule. The AAf and AAnf results are shown to converge to the TDSE results as the adiabatic parameters (37) and (59), respectively, tend to zero. The main difference between the adiabatic and TDSE results for few-cycle pulses at finite values of the parameters is caused by rescattering not accounted for by the present versions of AAf and AAnf. We mention that the present 1D model exaggerates the relative role of rescattering effects compared to the 3D case; see Refs. [44,56]. The usefulness of the theory is illustrated by the analysis of interference structures in partial PEMDs generated by almost monochromatic pulses and isotope effect in the distribution of channel ionization probabilities.

As an outlook, let us indicate three directions of possible generalizations of the present theory. Rescattering can be accounted for following the approach developed in Ref. [44]; this will be discussed elsewhere. Two other directions of interest for applications are the inclusion of the dissociation channel on the basis of the approach developed in a time-independent framework [41,42] and the extension of AAnf to 3D electronic motion using a method for calculating molecular SSs in an electric field developed in Refs. [61,67,68]. The latter extension will enable one to study the distribution of photoelectrons in the transverse component of their momentum with respect to the polarization axis not reproduced by the 1D model, which contains additional structural information, e.g., encoded in the strong-field photoelectron holography pattern [46]. The thus-generalized theory covering all the essential aspects of the electronic and nuclear dynamics will find applications in the analysis of strong-field processes in midinfrared [52] and terahertz [53] ranges, in which case solving the TDSE is not feasible.

ACKNOWLEDGMENTS

This work was supported in part by JSPS KAKENHI Grants No. 17F17901, No. 17K05597, and No. 19H00887. J.S. was supported as an International Research Fellow by the JSPS for the majority of this work. O.I.T. acknowledges support from the Russian Academic Excellence Project "5–100."

APPENDIX: NUMERICAL PROCEDURES

In this Appendix, the numerical methods used in this work are described. The main programs used for TDSE and SS calculations were implemented in FORTRAN, while postprocessing of data, plotting, and evaluation of the adiabatic approximations were done using PYTHON. Interfacing data between FORTRAN and PYTHON was partly done using NetCDF. We used the PYTHON libraries f90nml, NumPy, xarray, HoloViews, and Matplotlib extensively.

In the first section, we describe the programs used for solving the TDSE and obtaining observables from this solution. The following section describes how we implemented the adiabatic approximations. The last section gives numerical parameters for one of the most demanding calculations in this work and estimates of the computational time scaling for the three-body TDSE program.

1. Three-body TDSE

For propagating solutions to the three-body TDSE (8), we used the split-step Fourier method [69] with the sine discrete variable representation (sine-DVR) [70,71] functions as a basis set. In this section, we first describe the sine-DVR and then the split-step Fourier method. Finally, we describe how the scattering states were calculated and how the propagated solutions were projected onto those to obtain the ionization amplitudes.

a. Sine discrete variable representation

We will start by listing some of the central properties of the sine-DVR. In this subsection, we consider a 1D problem in a box $z_{\min} \leqslant z \leqslant z_{\max}$ of length $L = z_{\max} - z_{\min}$. The sine-DVR in this box consists of N functions given by

$$\pi_j(z) = \sum_{n=1}^{N} T_{nj}\phi_n(z), \;\; j = 1, \ldots, N, \tag{A1}$$

where the finite basis set representation (FBR) functions $\phi_n(z)$ are given by

$$\phi_n(z) = \sqrt{\frac{2}{L}} \sin\left(n\pi \frac{z - z_{\min}}{L}\right), \;\; n = 1, \ldots, N, \tag{A2}$$

and the transformation matrix from the FBR to the DVR functions is

$$T_{nj} = \sqrt{\frac{2}{N+1}} \sin\left(\pi \frac{nj}{N+1}\right). \tag{A3}$$

The FBR functions $\phi_n(z)$ are orthonormal with respect to integration in the box over the interval $[z_{\min}, z_{\max}]$. The DVR functions $\pi_j(z)$ are also orthonormal under the same norm. Integrals in the box can be approximated using the quadrature rule associated with the DVR for a smooth function $g(z)$ as

$$\int_{z_{\min}}^{z_{\max}} g(z)dz \approx \sum_j g(z_j)w, \tag{A4}$$

where the quadrature points and weight are given by

$$z_j = z_{\min} + \frac{j}{N+1}L, \tag{A5a}$$

$$w = \frac{L}{N+1}. \tag{A5b}$$

This leads to

$$\int_{z_{\min}}^{z_{\max}} \pi_i(z) f(z) \pi_j(z) dz \approx f(z_j)\delta_{ij}, \tag{A6}$$

where $f(z)$ is a smooth function and we used the property

$$\pi_i(z_j) = \sqrt{\frac{L}{N+1}}\delta_{ij}. \tag{A7}$$

The matrix elements of the kinetic energy $K = -\frac{1}{2m}\frac{\partial^2}{\partial z^2}$ can be expressed as

$$\int_{z_{\min}}^{z_{\max}} \pi_i(z) K \pi_j(z) dz = \frac{\pi^2}{2mL^2}\sum_{n=1}^{N} n^2 T_{in} T_{jn}. \tag{A8}$$

A wave function can be expanded in terms of the DVR functions

$$\psi(z) = \sum_{j=1}^{N} \psi_j \pi_j(z) \tag{A9a}$$

$$= \sum_{n=1}^{N} \phi_n \phi_n(z), \tag{A9b}$$

where

$$\phi_n = \sum_{j=1}^{N} T_{nj}\psi_j. \tag{A10}$$

The transformation in Eq. (A10) is up to a constant of the same form as the type-I discrete sine transform (DST-I) [72]. This allows us to take advantage of optimized DST implementations for performing this transformation. In our program, we used the FFTW library [72]. Since T_{nj} is orthogonal and symmetric, the inverse transformation is also a DST-I. Note that all the FBR and DVR functions are zero at $z_{\min}$ and $z_{\max}$.

In this work, we found that the expansion by DVR functions converges very slowly to the wave function for light nuclear masses when using the internuclear potential (85) with $D = 0$. This is caused by this potential having a divergence at $R = 0$, where the wave function therefore behaves as a noninteger power of R. Such a wave function is not well described by the DVR functions, since these functions all go to zero linearly. For this reason, we used a set of potential parameters with $D > 0$ to consider light nuclear masses.

b. Time propagation

Here we describe the split-step Fourier method [69] used for the time propagation of the wave function. We approximate the time evolution operator $U(t + \Delta t, t)$ from t to $t + \Delta t$ by the short-time propagator

$$U(t + \Delta t, t) = e^{-iH(t+\Delta t/2)\Delta t} + O(\Delta t^3), \tag{A11}$$

where $H(t) = H_0 + F(t)x$ is the time-dependent Hamiltonian (8). We further split the short-time propagator in purely coordinate-dependent potential $V(x, R, t) = V(x; R) + U_{\text{ion}}(R) + F(t)x$ and purely momentum-dependent kinetic $K = -\frac{1}{2\mu}\frac{\partial^2}{\partial R^2} - \frac{1}{2m}\frac{\partial^2}{\partial x^2}$ parts,

$$U(t + \Delta t, t) = e^{-i\frac{1}{2}K\Delta t} e^{-iV(x,R,t+\Delta t/2)\Delta t} e^{-i\frac{1}{2}K\Delta t} + O(\Delta t^3). \tag{A12}$$

We used a product basis of the DVR functions $\pi_j(x)\pi_l(R)$ and the corresponding FBR functions $\phi_n(x)\phi_m(R)$. The product FBR functions $\phi_n(x)\phi_m(R)$ are eigenfunctions of the kinetic energy, meaning that the corresponding matrix is diagonal in this representation,

$$\int_{x_{\min}}^{x_{\max}} \int_{R_{\min}}^{R_{\max}} \phi_n(x)\phi_m(R) K \phi_o(x)\phi_p(R) dR dx = \left(\frac{n^2\pi^2}{2mL_x^2} + \frac{m^2\pi^2}{2\mu L_R^2}\right)\delta_{no}\delta_{mp}, \tag{A13}$$

where $L_x = x_{\max} - x_{\min}$ and $L_R = R_{\max} - R_{\min}$ are the sizes of the box used in the x and R coordinate respectively. Using Eq. (A6), we see that within the quadrature approximation the potential matrix is likewise diagonal in the DVR representation

$$\int_{x_{\min}}^{x_{\max}} \int_{R_{\min}}^{R_{\max}} \pi_i(x)\pi_k(R) V(x, R, t) \pi_j(x)\pi_l(R) dR dx \approx V(x_i, R_k, t)\delta_{ij}\delta_{kl}. \tag{A14}$$

The wave function is propagated in time by first transforming to the FBR using the DST-I, applying the $e^{-i\frac{1}{2}K\Delta t}$ operator, transforming back to the DVR again using DST-I, applying the $e^{-iV(x,R,t+\Delta t/2)\Delta t}$ operator, then transforming back to the FBR basis, applying the next operator and so forth.

c. Bound states

In order to find the bound states, we diagonalized the field-free Hamiltonian matrix in the DVR. The ground state was used as an initial state for the time propagation, and the full set of bound states were used to obtain the final bound-state populations. We calculated the potential and kinetic energy matrices using Eqs. (A14) and (A8) respectively. Since the kinetic energy matrix is a full matrix, diagonalizing the Hamiltonian on the full grid used in the time propagation quickly becomes unfeasible even for moderate box sizes. However, since we only consider finite-range potentials here, there are only a finite number of bound states, and these are confined in a smaller region. The diagonalization was sped up significantly by only using grid points in this smaller region containing all the bound states. The bound-state wave functions were subsequently extended to the full time propagation grid by putting them to zero outside this inner region. We used the FORTRAN library LAPACK to perform the diagonalization.

Imaginary time propagation is an alternative method for finding the initial bound state when using the split-step Fourier method. However, it is very difficult to obtain excited states with this method. Additionally, by using diagonalization there is no need to worry about convergence with respect to the imaginary time step size.

d. Scattering states

Three-body scattering states (4) were calculated with a method similar to that in Ref. [73], although here we used rectangular coordinates x and R rather than the hyperspherical coordinates used there.

Because of the mirror symmetry of the system about $x = 0$, we calculated even and odd states separately on the half-axis $x \geqslant 0$. We express the asymptotic boundary condition for

these even-odd scattering states in terms of the K matrix as

$$\Psi_v^{(e,o)}(x,R;E) = f^{(s)}(x;k_v(E))\chi_v(R) + \sum_{v'} f^{(c)}(x;k_{v'}(E))\chi_{v'}(R)K_{v'v}^{(e,o)}(E), \tag{A15}$$

where

$$f^{(s)}(x;k) = \sqrt{\frac{m}{k}}\sin(kx), \tag{A16a}$$

$$f^{(c)}(x;k) = \sqrt{\frac{m}{k}}\cos(kx), \tag{A16b}$$

with the momenta being $k_v(E) = \sqrt{2m(E-\varepsilon_v)}$. The even-odd K matrices are related to the S matrix from Eq. (6) for $k > 0$ by

$$S_{v'v}^{\mp}(-k) = S_{v'v}^{\pm}(k) = \frac{1}{2}\sqrt{\frac{k}{m}}\left[S_{v'v}^{(e)}(E_v(k)) \pm S_{v'v}^{(o)}(E_v(k))\right], \tag{A17a}$$

$$S^{(e,o)}(E) = [1 + iK^{(e,o)}(E)][1 - iK^{(e,o)}(E)]^{-1}, \tag{A17b}$$

where $E_v(k) = \frac{1}{2m}k^2 + \varepsilon_v$ [as in Eq. (5)]. The *in*- and *out*-scattering states can be constructed from the even-odd states, again for $k > 0$, by

$$\Phi_v^{(+)}(x,R;\pm k) = -\frac{1}{2}\sqrt{\frac{k}{m}}\left[\tilde{\Psi}_v^{(e)}(x,R;E_v(k)) \mp \tilde{\Psi}_v^{(o)}(x,R;E_v(k))\right], \tag{A18a}$$

$$\Phi_v^{(-)}(x,R;\pm k) = \frac{1}{2}\sqrt{\frac{k}{m}}\sum_{v'}\left[\tilde{\Psi}_{v'}^{(e)}(x,R;E_v(k))[S^{(e)}(E_v(k))]_{v'v}^{-1} \pm \tilde{\Psi}_{v'}^{(o)}(x,R;E_v(k))[S^{(o)}(E_v(k))]_{v'v}^{-1}\right], \tag{A18b}$$

where

$$\tilde{\Psi}_v^{(e,o)}(x,R;E) = 2i\sum_{v'}\Psi_{v'}^{(e,o)}(x,R;E)[1 - iK^{(e,o)}(E)]_{v'v}^{-1}. \tag{A19}$$

Here the $\Psi_{v'}^{(e,o)}(x,R;E)$ functions are extended to the whole x axis by using the even-odd symmetry about $x = 0$.

In order to calculate the K matrices and scattering wave functions, we used the R-matrix propagation method [74]. The R matrix $\mathcal{R}_{v\mu}(x)$ is defined by

$$\int_0^\infty \Phi_v(x,R)\Psi(x,R;E)dR = \sum_\mu \mathcal{R}_{v\mu}(x)\int_0^\infty \Phi_\mu(x,R)\frac{\partial\Psi(x,R;E)}{\partial x}dR, \tag{A20}$$

where the adiabatic channel functions $\Phi_\mu(R;x)$ and the eigenvalues $U_\mu(x)$ are solutions to the eigenvalue problem,

$$[\mathcal{U}(x) - U_\mu(x)]\Phi_\mu(R;x) = 0, \tag{A21a}$$

$$\mathcal{U}(x) = -\frac{1}{2\mu}\frac{\partial^2}{\partial R^2} + U_{\rm ion}(R) + V(x;R), \tag{A21b}$$

for fixed values of x, subject to the boundary conditions $\Phi_\mu(R=0;x) = \Phi_\mu(R=\infty;x) = 0$. We solved this equation by diagonalizing the $\mathcal{U}(x)$ operator expressed in the sine-DVR. The R-matrix propagation was performed by first dividing the x coordinate into a number of sectors. The R matrix was then propagated through each of these sectors using the slow variable discretization (SVD) [75] method with the Legendre-DVR functions. Details of the computational method for the propagation is described in the Appendix of Ref. [61].

The R matrix for even (odd) states was propagated from $x = 0$ with the initial condition $R(0) = 0$ ($R(0) = \infty$) to the matching point x_m. This matching point was chosen to be sufficiently far from the origin such that the potential $V(x;R)$ and hence any couplings between different adiabatic channels had vanished. In this region, the adiabatic channel functions $\Phi_\mu(R;x)$ coincide with the molecular ionic eigenfunctions $\chi_v(R)$. The K matrix can be expressed in terms of the R matrix as

$$K^{(e,o)}(E) = -[F^{(c)} - \mathcal{R}^{(e,o)}(x_m)D^{(c)}]^{-1} \times [F^{(s)} - \mathcal{R}^{(e,o)}(x_m)D^{(s)}], \tag{A22}$$

where the components of the $F^{(s,c)}$ and $D^{(s,c)}$ matrices are

$$F_{\mu v}^{(s,c)} = \delta_{\mu v}f^{(s,c)}(x;k_v(E))|_{x=x_m}, \tag{A23a}$$

$$D_{\mu v}^{(s,c)} = \delta_{\mu v}\frac{\partial}{\partial x}f^{(s,c)}(x;k_v(E))|_{x=x_m}. \tag{A23b}$$

This expression was obtained by matching using the asymptotic form of the wave function (A15) and the definition of the R matrix (A20).

e. Projection of the TDSE wave function onto scattering states

The ionization amplitude (11) is obtained by projection of the TDSE wave function onto the scattering states. The integration was done using the quadrature rules associated with the scattering grid. The TDSE wave function was put on the scattering grid by evaluating the 2D version of Eq. (A9b), which gives better accuracy than, e.g., spline interpolation.

2. Adiabatic approximations

SSs are essential components needed for implementing the AAs. The SSs used in the AAf were calculated using the R-matrix propagation method in complex variables. Details of the method are described in Ref. [40]. The electronic SSs (60) used in AAnf were found with the same method, reduced to the 1D case. In the following subsection, we mention some details regarding the evaluation of the ionization amplitude applicable to both AAf and AAnf. For the AAnf, we additionally need solutions to the nuclear TDSE (66), described in the subsequent subsection.

a. Evaluation of ionization amplitude expressions

The ionization amplitudes in both AAf and AAnf are obtained for any given value of k by using the saddle points that are defined by Eq. (55). The number of saddle points depends on the pulse shape and k. For the few-cycle pulse

[Eqs. (82) and (84)], there are infinitely many for k near zero, but most of the significant contributions to the ionization amplitude comes from around the peak of pulse. We therefore only need to use a finite number of saddle points, and we consider this number as a convergence parameter.

The calculation of the AAs' ionization amplitudes was performed in PYTHON, using Brent's method for finding the saddle points. For keeping track of all the indices involved, the PYTHON library xarray was useful.

b. Nuclear TDSE

We expand the nuclear wave function in terms of nuclear bound states (69) in the interaction picture as

$$\Psi(R,t) = \sum_n c_n(t)\Psi_n(R)e^{-iE_n^{\mathrm{BO}}t}. \tag{A24}$$

Using this, we express the nuclear TDSE (66) in terms of the time-dependent coefficients $c_n(t)$ as

$$i\frac{\partial}{\partial t}c_n(t) = \sum_{n'} e^{i(E_n^{\mathrm{BO}}-E_{n'}^{\mathrm{BO}})t}\,\Delta E_{nn'}(F(t))c_{n'}(t), \tag{A25}$$

where

$$\Delta E_{nn'}(F) = \int_0^\infty \Psi_n(R)[E_e(R,F) - E_e(R,0)]\Psi_{n'}(R)dR. \tag{A26}$$

We prepare the $\Delta E_{nn'}(F)$ matrix elements at a number of fixed values of F by solving Eq. (69) using the sine-DVR, and then using the associated quadrature to evaluate the integrals in R. The electronic SS energies $E_e(R,F)$ that enter in this integral were calculated using the method referred to above. We then propagate Eq. (A25) through the pulse using the fixed-step fourth-order Runge-Kutta algorithm from Ref. [76], where we used the spline interpolation algorithm from the same reference to obtain $\Delta E_{nn'}(F)$ at any needed values of F.

3. Numerics

a. Numerical parameters and computational performance

Here we give an example of the parameters used in one of the most demanding three-body TDSE calculations, namely for the half-cycle, $M = 1836$, $F_0 = 0.2$, $T = 150$ calculation, shown in the lower right panel of Figs. 8, 9, and 10. The box size in x was $L_x = 13\,200$ with $N_x = 1.5\times10^5$ points in x. In R, these parameters were $L_R = 6.0$ and $N_R = 60$. In total, this calculation used around $N = N_xN_R = 9\times10^6$ grid points. The time-step size was $\Delta t = 0.007$ for a total propagation time of 750, so around $N_t = 10^5$ time steps were taken. With these parameters, the time propagation took about 1 day and 16 h on a 36-core Intel Xeon 6140 machine. Finding bound states through diagonalization for these parameters took around 19 min. For finding scattering states, we used comparable grid spacing and 60 adiabatic channels, and the execution time for 200 energies was around 3 h. Solving the nuclear TDSE Eq. (66) took about 1 min for this case, although finding SS energies that enters that calculation took about 5 h. It should be noted though that the SS calculation does not have to be repeated for different field parameters. As long as the system is the same, the same set of SS energies can be used, whereas the three-body TDSE calculation has to be repeated whenever the field is changed.

The convergence of our calculations was tested by varying all relevant numerical parameters a significant amount and seeing that such variation did not visibly alter the final physical observables in the figures.

b. Scaling of parameters

Here we provide estimates for how the computational time T_{comp} of our three-body TDSE program scales with the physical parameters of the problem, namely the maximal amplitude F_0, the timescale T_f, and the total duration of the laser pulse T_{tot}.

As a first step, we examine how the numerical parameters scale in terms of the physical parameters in the adiabatic regime. Such estimates are also useful for choosing numerical parameters when physical parameters are varied. The maximal momentum of the electrons scales as

$$k_{\max} \propto F_0T_f. \tag{A27}$$

L_x is determined by the product of the velocity of the fastest electron $\sim k_{\max}$, and the amount of time it has for moving $\sim T_{\mathrm{tot}}$. Thus, we have

$$L_x \propto k_{\max}T_{\mathrm{tot}} \propto F_0T_fT_{\mathrm{tot}}. \tag{A28}$$

The grid size $\Delta x = L_x/N_x$ should be inversely proportional to the maximal momentum, so that

$$\Delta x \propto k_{\max}^{-1} \propto F_0^{-1}T_f^{-1}. \tag{A29}$$

The time step size Δt should scale inversely with the maximal energy of the electrons, namely

$$\Delta t \propto k_{\max}^{-2} \propto F_0^{-2}T_f^{-2}. \tag{A30}$$

For a 1D DST, the computational time scales as $N\log N$, where N is the number of points. The evaluations of the potential and exponentials are potentially quite time-consuming, but they only scale as N. For the following estimate, we will assume that the DST is the most time-consuming part of our program. We perform two DSTs for each time step, so the total computational time should scale linearly with the number of time steps N_t. Using the scalings

$$N_x \approx L_x/\Delta x \propto F_0^2T_f^2T_{\mathrm{tot}}, \tag{A31a}$$

$$N_t \approx T_{\mathrm{tot}}/\Delta t \propto F_0^2T_f^2T_{\mathrm{tot}}, \tag{A31b}$$

we arrive at following scaling for the computational time:

$$T_{\mathrm{comp}} \propto N_tN_x\log N_xN_R\log N_R \propto F_0^4T_f^4T_{\mathrm{tot}}^2\log\left(F_0^2T_f^2T_{\mathrm{tot}}\right), \tag{A32}$$

where we assumed that the number of points in the R-coordinate N_R is independent of the physical parameters, since in the model considered in this work, the wave function is confined by the potential in this direction.

As an example, let us consider the few-cycle pulse (84) for which $T_{\mathrm{tot}} \propto T$ and $T_f \sim \pi/\omega = T/2n_{\mathrm{oc}}$. For a case in which we increase the duration T while keeping the number of cycles constant, we see that $T_{\mathrm{tot}} \propto T$ and $T_f \propto T$, so $T_{\mathrm{comp}} \propto F_0^4T^6\log(F_0^2T^3)$. If we instead increase the duration of the

pulse while keeping the frequency constant, then $T_{\rm tot} \propto T$, but T_f will not change. So we have $T_{\rm comp} \propto F_0^4 T^2 \log(F_0^2 T)$. Note that in physical regimes other than the adiabatic one, there would most likely be different scalings of computational time.

[1] F. Krausz and M. Ivanov, Attosecond physics, Rev. Mod. Phys. **81**, 163 (2009).

[2] S. Chelkowski, T. Zuo, O. Atabek, and A. D. Bandrauk, Dissociation, ionization, and Coulomb explosion of H_2^+ in an intense laser field by numerical integration of the time-dependent Schrödinger equation, Phys. Rev. A **52**, 2977 (1995).

[3] S. Chelkowski, A. Conjusteau, T. Zuo, and A. D. Bandrauk, Dissociative ionization of H_2^+ in an intense laser field: Charge-resonance-enhanced ionization, Coulomb explosion, and harmonic generation at 600 nm, Phys. Rev. A **54**, 3235 (1996).

[4] K. C. Kulander, F. H. Mies, and K. J. Schafer, Model for studies of laser-induced nonlinear processes in molecules, Phys. Rev. A **53**, 2562 (1996).

[5] E. A. Volkova, A. M. Popov, and O. V. Tikhonova, Two-particle one-dimensional model of the hydrogen molecular ion in an ultrashort laser pulse, Zh. Eksp. Teor. Fiz. **110**, 1616 (1996) [Sov. Phys. - JETP **83**, 889 (1996)].

[6] S. Chelkowski, C. Foisy, and A. D. Bandrauk, Electron-nuclear dynamics of multiphoton H_2^+ dissociative ionization in intense laser fields, Phys. Rev. A **57**, 1176 (1998).

[7] I. Kawata, H. Kono, and Y. Fujimura, Adiabatic and diabatic responses of H_2^+ to an intense femtosecond laser pulse: Dynamics of the electronic and nuclear wave packet, J. Chem. Phys. **110**, 11152 (1999).

[8] S. Chelkowski, P. B. Corkum, and A. D. Bandrauk, Femtosecond Coulomb Explosion Imaging of Vibrational Wave Functions, Phys. Rev. Lett. **82**, 3416 (1999).

[9] V. Roudnev, B. D. Esry, and I. Ben-Itzhak, Controlling HD^+ and H_2^+ Dissociation with the Carrier-Envelope Phase Difference of an Intense Ultrashort Laser Pulse, Phys. Rev. Lett. **93**, 163601 (2004).

[10] V. Roudnev and B. D. Esry, HD^+ photodissociation in the scaled coordinate approach, Phys. Rev. A **71**, 013411 (2005).

[11] M. Lein, Attosecond Probing of Vibrational Dynamics with High-Harmonic Generation, Phys. Rev. Lett. **94**, 053004 (2005).

[12] S. Chelkowski, A. D. Bandrauk, A. Staudte, and P. B. Corkum, Dynamic nuclear interference structures in the Coulomb explosion spectra of a hydrogen molecule in intense laser fields: Reexamination of molecular enhanced ionization, Phys. Rev. A **76**, 013405 (2007).

[13] G. K. Paramonov, Vibrational excitation of simple molecular ions in resonant and under-resonant strong laser fields: Dissociation and ionization of *ppe* and *pde*; laser-enhanced nuclear fusion in $dd\mu$ and $dt\mu$, Chem. Phys. **338**, 329 (2007).

[14] F. He, A. Becker, and U. Thumm, Strong-Field Modulated Diffraction Effects in the Correlated Electron-Nuclear Motion in Dissociating H_2^+, Phys. Rev. Lett. **101**, 213002 (2008).

[15] C. B. Madsen, F. Anis, L. B. Madsen, and B. D. Esry, Multiphoton Above Threshold Effects in Strong-Field Fragmentation, Phys. Rev. Lett. **109**, 163003 (2012).

[16] R. E. F. Silva, F. Catoire, P. Rivière, H. Bachau, and F. Martín, Correlated Electron and Nuclear Dynamics in Strong Field Photoionization of H_2^+, Phys. Rev. Lett. **110**, 113001 (2013).

[17] F. Morales, P. Rivière, M. Richter, A. Gubaydullin, M. Ivanov, O. Smirnova, and F. Martín, High harmonic spectroscopy of electron localization in the hydrogen molecular ion, J. Phys. B **47**, 204015 (2014).

[18] C. Huang, O. I. Tolstikhin, and T. Morishita, Strong-field subcycle control of dissociation dynamics via exceptional points of molecules in an electric field, Phys. Rev. A **95**, 063416 (2017).

[19] G. K. Paramonov, T. Klamroth, H. Z. Lu, and A. D. Bandrauk, Quantum dynamics, isotope effects, and power spectra of H_2^+ and HD^+ excited to the continuum by strong one-cycle laser pulses: Three-dimensional non-Born-Oppenheimer simulations, Phys. Rev. A **98**, 063431 (2018).

[20] H. Xu, T.-Y. Xu, F. He, D. Kielpinski, R. T. Sang, and I. V. Litvinyuk, Effect of nuclear mass on carrier-envelope-phase-controlled electron localization in dissociating molecules, Phys. Rev. A **89**, 041403(R) (2014).

[21] S. Baker, J. S. Robinson, C. A. Haworth, H. Teng, R. A. Smith, C. C. Chirilă, M. Lein, J. W. G. Tisch, and J. P. Marangos, Probing proton dynamics in molecules on an attosecond time scale, Science **312**, 424 (2006).

[22] A. Staudte, D. Pavičić, S. Chelkowski, D. Zeidler, M. Meckel, H. Niikura, M. Schöffler, S. Schössler, B. Ulrich, P. P. Rajeev, T. Weber, T. Jahnke, D. M. Villeneuve, A. D. Bandrauk, C. L. Cocke, P. B. Corkum, and R. Dörner, Attosecond Strobing of Two-Surface Population Dynamics in Dissociating H_2^+, Phys. Rev. Lett. **98**, 073003 (2007).

[23] J. Wu, M. Kunitski, M. Pitzer, F. Trinter, L. P. H. Schmidt, T. Jahnke, M. Magrakvelidze, C. B. Madsen, L. B. Madsen, U. Thumm, and R. Dörner, Electron-Nuclear Energy Sharing in Above-Threshold Multiphoton Dissociative Ionization of H_2, Phys. Rev. Lett. **111**, 023002 (2013).

[24] P. Lu, W. Zhang, X. Gong, Q. Song, K. Lin, Q. Ji, J. Ma, F. He, H. Zeng, and J. Wu, Electron-nuclear correlation in above-threshold double ionization of molecules, Phys. Rev. A **95**, 033404 (2017).

[25] W. Zhang, X. Gong, H. Li, P. Lu, F. Sun, Q. Ji, K. Lin, J. Ma, H. Li, J. Qiang *et al.*, Electron-nuclear correlated multiphoton-route to Rydberg fragments of molecules, Nat. Commun. **10**, 757 (2019).

[26] D. G. Arbó, S. Yoshida, E. Persson, K. I. Dimitriou, and J. Burgdörfer, Interference Oscillations in the Angular Distribution of Laser-Ionized Electrons Near Ionization Threshold, Phys. Rev. Lett. **96**, 143003 (2006).

[27] T. Morishita, Z. Chen, S. Watanabe, and C. D. Lin, Two-dimensional electron momentum spectra of argon ionized by short intense lasers: Comparison of theory with experiment, Phys. Rev. A **75**, 023407 (2007).

[28] A. N. Grum-Grzhimailo, B. Abeln, K. Bartschat, D. Weflen, and T. Urness, Ionization of atomic hydrogen in strong infrared laser fields, Phys. Rev. A **81**, 043408 (2010).

[29] I. A. Ivanov and A. S. Kheifets, Strong-field ionization of He by elliptically polarized light in attoclock configuration, Phys. Rev. A **89**, 021402(R) (2014).

[30] M. Ohmi, O. I. Tolstikhin, and T. Morishita, Analysis of a shift of the maximum of photoelectron momentum distributions

generated by intense circularly polarized pulses, Phys. Rev. A **92**, 043402 (2015).

[31] X.-F. Hou, L.-Y. Peng, Q.-C. Ning, and Q. Gong, Attosecond streaking of molecules in the low-energy region studied by a wave-function splitting scheme, J. Phys. B **45**, 074019 (2012).

[32] O. I. Tolstikhin and T. Morishita, Strong-field ionization, rescattering, and target structure imaging with vortex electrons, Phys. Rev. A **99**, 063415 (2019).

[33] C.-N. Liu, A. Hishikawa, and T. Morishita, Two-electron dynamics in nonlinear double excitation of helium by intense ultrashort extreme-ultraviolet pulses, Phys. Rev. A **86**, 053426 (2012).

[34] J. M. N. Djiokap, S. X. Hu, W.-C. Jiang, L.-Y. Peng, and A. F. Starace, Enhanced asymmetry in few-cycle attosecond pulse ionization of He in the vicinity of autoionizing resonances, New J. Phys. **14**, 095010 (2012).

[35] X. Urbain, B. Fabre, E. M. Staicu-Casagrande, N. de Ruette, V. M. Andrianarijaona, J. Jureta, J. H. Posthumus, A. Saenz, E. Baldit, and C. Cornaggia, Intense-Laser-Field Ionization of Molecular Hydrogen in the Tunneling Regime and its Effect on the Vibrational Excitation of H_2^+, Phys. Rev. Lett. **92**, 163004 (2004).

[36] O. I. Tolstikhin, H. J. Wörner, and T. Morishita, Effect of nuclear motion on tunneling ionization rates of molecules, Phys. Rev. A **87**, 041401(R) (2013).

[37] X. Wang, H. Xu, A. Atia-Tul-Noor, B. T. Hu, D. Kielpinski, R. T. Sang, and I. V. Litvinyuk, Isotope Effect in Tunneling Ionization of Neutral Hydrogen Molecules, Phys. Rev. Lett. **117**, 083003 (2016).

[38] O. I. Tolstikhin and L. B. Madsen, Retardation Effects and the Born-Oppenheimer Approximation: Theory of Tunneling Ionization of Molecules Revisited, Phys. Rev. Lett. **111**, 153003 (2013).

[39] O. I. Tolstikhin, T. Morishita, and L. B. Madsen, Theory of tunneling ionization of molecules: Weak-field asymptotics including dipole effects, Phys. Rev. A **84**, 053423 (2011).

[40] J. Svensmark, O. I. Tolstikhin, and L. B. Madsen, Coulomb and dipole effects in tunneling ionization of molecules including nuclear motion, Phys. Rev. A **91**, 013408 (2015).

[41] J. Svensmark, O. I. Tolstikhin, and L. B. Madsen, Theory of dissociative tunneling ionization, Phys. Rev. A **93**, 053426 (2016).

[42] J. Svensmark, O. I. Tolstikhin, and L. B. Madsen, Bound and continuum energy distributions of nuclear fragments resulting from tunneling ionization of molecules, Phys. Rev. A **97**, 033408 (2018).

[43] O. I. Tolstikhin and T. Morishita, Weak-field versus Born-Oppenheimer asymptotics in the theory of tunneling ionization of molecules, Phys. Rev. A **95**, 033410 (2017).

[44] O. I. Tolstikhin and T. Morishita, Adiabatic theory of ionization by intense laser pulses: Finite-range potentials, Phys. Rev. A **86**, 043417 (2012).

[45] K. Liu, S. Luo, M. Li, Y. Li, Y. Feng, B. Du, Y. Zhou, P. Lu, and I. Barth, Detecting and Characterizing the Nonadiabaticity of Laser-Induced Quantum Tunneling, Phys. Rev. Lett. **122**, 053202 (2019).

[46] Y. Zhou, O. I. Tolstikhin, and T. Morishita, Near-Forward Rescattering Photoelectron Holography in Strong-Field Ionization: Extraction of the Phase of the Scattering Amplitude, Phys. Rev. Lett. **116**, 173001 (2016).

[47] T. Morishita and O. I. Tolstikhin, Adiabatic theory of strong-field photoelectron momentum distributions near a backward rescattering caustic, Phys. Rev. A **96**, 053416 (2017).

[48] H. Geiseler, N. Ishii, K. Kaneshima, F. Geier, T. Kanai, O. I. Tolstikhin, T. Morishita, and J. Itatani, Carrier-envelope phase mapping in laser-induced electron diffraction, Phys. Rev. A **94**, 033417 (2016).

[49] Y. Ito, M. Okunishi, T. Morishita, O. I. Tolstikhin, and K. Ueda, Rescattering photoelectron spectroscopy of heterodiatomic molecules with an analytical returning photoelectron wave packet, Phys. Rev. A **97**, 053411 (2018).

[50] M. Okunishi, Y. Ito, V. Sharma, S. Aktar, K. Ueda, R. R. Lucchese, A. I. Dnestryan, O. I. Tolstikhin, S. Inoue, H. Matsui, and T. Morishita, Rescattering photoelectron spectroscopy of the CO_2 molecule: Progress towards experimental discrimination between theoretical target-structure models, Phys. Rev. A **100**, 053404 (2019).

[51] V. N. T. Pham, O. I. Tolstikhin, and T. Morishita, Images of molecular orbitals in strong-field photoelectron momentum distributions generated by circularly polarized pulses, Phys. Rev. A **99**, 013428 (2019).

[52] B. Wolter, M. G. Pullen, M. Baudisch, M. Sclafani, M. Hemmer, A. Senftleben, C. D. Schröter, J. Ullrich, R. Moshammer, and J. Biegert, Strong-Field Physics with Mid-IR Fields, Phys. Rev. X **5**, 021034 (2015).

[53] X. Zhang, A. Shkurinov, and Y. Zhang, Extreme terahertz science, Nat. Photon. **11**, 16 (2017).

[54] L. D. Landau and E. M. Lifshitz, *Quantum Mechanics, Non-relativistic Theory* (Pergamon, Oxford, UK, 1977).

[55] R. P. Feynman and A. R. Hibbs, *Quantum Mechanics and Path Integrals* (McGraw-Hill, New York, 1965).

[56] O. I. Tolstikhin, T. Morishita, and S. Watanabe, Adiabatic theory of ionization of atoms by intense laser pulses: One-dimensional zero-range-potential model, Phys. Rev. A **81**, 033415 (2010).

[57] J. Li and U. Thumm, Semiclassical approach for solving the time-dependent Schrödinger equation in spatially inhomogeneous electromagnetic pulses, Phys. Rev. A **101**, 013411 (2020).

[58] G. D. Dickenson, M. L. Niu, E. J. Salumbides, J. Komasa, K. S. E. Eikema, K. Pachucki, and W. Ubachs, Fundamental Vibration of Molecular Hydrogen, Phys. Rev. Lett. **110**, 193601 (2013).

[59] A. J. F. Siegert, On the derivation of the dispersion formula for nuclear reactions, Phys. Rev. **56**, 750 (1939).

[60] O. I. Tolstikhin, V. N. Ostrovsky, and H. Nakamura, Siegert pseudostate formulation of scattering theory: One-channel case, Phys. Rev. A **58**, 2077 (1998).

[61] P. A. Batishchev, O. I. Tolstikhin, and T. Morishita, Atomic Siegert states in an electric field: Transverse momentum distribution of the ionized electrons, Phys. Rev. A **82**, 023416 (2010).

[62] H. Wind, Electron energy for H_2^+ in the ground state, J. Chem. Phys. **42**, 2371 (1965).

[63] K. Pachucki, Born-Oppenheimer potential for H_2, Phys. Rev. A **82**, 032509 (2010).

[64] E. A. Gislason, Series expansions for Franck-Condon factors. I. Linear potential and the reflection approximation, J. Chem. Phys. **58**, 3702 (1973).

[65] P. Agostini, F. Fabre, G. Mainfray, G. Petite, and N. K. Rahman, Free-Free Transitions Following Six-Photon Ionization of Xenon Atoms, Phys. Rev. Lett. **42**, 1127 (1979).

[66] L. Yue and L. B. Madsen, Inter- and intracycle interference effects in strong-field dissociative ionization, Phys. Rev. A **93**, 031401(R) (2016).

[67] L. Hamonou, T. Morishita, and O. I. Tolstikhin, Molecular Siegert states in an electric field, Phys. Rev. A **86**, 013412 (2012).

[68] V. N. T. Pham, O. I. Tolstikhin, and T. Morishita, Molecular Siegert states in an electric field. II. Transverse momentum distribution of the ionized electrons, Phys. Rev. A **89**, 033426 (2014).

[69] M. Feit, J. Fleck, and A. Steiger, Solution of the Schrödinger equation by a spectral method, J. Comput. Phys. **47**, 412 (1982).

[70] J. C. Light, I. P. Hamilton, and J. V. Lill, Generalized discrete variable approximation in quantum mechanics, J. Chem. Phys. **82**, 1400 (1985).

[71] J. T. Muckerman, Some useful discrete variable representations for problems in time-dependent and time-independent quantum mechanics, Chem. Phys. Lett. **173**, 200 (1990).

[72] M. Frigo and S. G. Johnson, The design and implementation of FFTW3, Proc. IEEE **93**, 216 (2005).

[73] O. I. Tolstikhin and C. Namba, *CTBC: A Program to Solve the Colinear Three-Body Coulomb Problem; Bound States and Scattering below the Three-body Disintegration Threshold* (National Institute for Fusion Science, Toki, Japan, 2003).

[74] K. Baluja, P. Burke, and L. Morgan, R-matrix propagation program for solving coupled second-order differential equations, Comput. Phys. Commun. **27**, 299 (1982).

[75] O. I. Tolstikhin, S. Watanabe, and M. Matsuzawa, "Slow" variable discretization: A novel approach for Hamiltonians allowing adiabatic separation of variables, J. Phys. B **29**, L389 (1996).

[76] W. Press, S. Teukolsky, W. Vetterling, and B. Flannery, *Numerical Recipes in Fortran 77: The Art of Scientific Computing* (Cambridge University Press, New York, 1992).